Article:
Hu, T., Yang, R., Wang, T. et al. (2026) Field evaluation of a ground-source heat pump system for frost heave control in high-speed railway subgrades. Energy, 344. 139850. ISSN: 0360-5442

https://doi.org/10.1016/j.energy.2025.139850

Development of a Geothermal Heat Pump System to Protect Against Railway Subgrade Frost Heave

Tianfei Hu [1], Rui Yang [1], Tengfei Wang [2,*], Zurun Yue [1], David P. Connolly [3], Yan Liu [4], Yifei Yuan [1]

1. State Key Laboratory of Mechanical Behavior and System Safety of Traffic Engineering Structures, Shijiazhuang Tiedao University, Shijiazhuang, 050043, China
2. Key Laboratory of High-Speed Railway Engineering (Southwest Jiaotong University), Ministry of Education, Chengdu, 610031, China
3. School of Civil Engineering, University of Leeds, Leeds LS2 9JT, UK
4. China Construction Eighth Engineering Division Co., Ltd., Shanghai, 200112, China

*Corresponding author: w@swjtu.edu.cn

Abstract

Subgrade frost heave is a persistent threat to railway operations in cold regions because it causes track misalignments and uneven support, potentially leading to safety risks. Thus, to actively mitigate frost heave, this paper proposes a novel ground-source heat pump (GSHP) system that uses shallow geothermal energy to heat frost-susceptible railway subgrade zones. The system comprises of vertical heat-collector pipes (evaporators), horizontally buried heat-supply pipes (condensers) and surface heat-pump units. To demonstrate the system, a 20 meter test section was constructed on a high-speed railway and monitored over a winter period. Prior to installation, dynamic heat-load analysis showed that the expected maximum subgrade heat load was 1,183 W/m with an average of 596 W/m. Therefore ten GSHP units rated at 1,200 W were installed at 2.0-m longitudinal spacing at a depth of 0.95 m. An intermittent heating schedule of, 2.5 h ON / 0.5 h OFF was used, resulting in the heat-supply pipes maintaining a mean outlet temperature of 18.7 °C throughout the heating period. This

resulted in frost depths being confined to 70–83 cm at the track center and 34–44 cm at the track shoulder. No frost-heave displacement exceeding tolerance thresholds was detected. In contrast, for the subgrade section that remained untreated, the maximum frost depths reached 195 cm (track center) and 224 cm (shoulder center), and the maximum upward displacement of the track due to frost heave was 6.2 mm. These field results demonstrate that GSHP-based active heating has the potential to substantially reduce frost depth, elevate minimum soil temperatures in the freezing zone, and reduce frost-heave-induced track irregularities. ~~The approach offers a practical mitigation strategy for high-speed railways operating in severe cold regions.~~

Keywords: subgrade frost heave; active heating; ground-source heat pump; frost depth; soil temperature; high-speed railway

1. Introduction

Seasonally frozen soils can undergo frost-heave displacement in winter, leading to differential settlement and cracking. On transport infrastructure, for example a railway, this deformation leads to track misalignments and may induce safety hazards such as fastener failure, thereby affecting rolling stock operation [1, 2]. Because track geometry for high-speed lines must be controlled to the millimeter scale, frost heave poses a persistent concern.

Although frost-resistant measures such as graded gravel, full-section waterproofing layers, and cement-stabilization are widely applied, frost heave continues to be a principal cause of track irregularities in cold-region subgrades [3–5]. In northern China, high-speed railways managed by the Harbin, Shenyang, Beijing, Taiyuan, Hohhot, and Lanzhou Railway Bureaus collectively experience approximately 5,000 frost-damaged sites each year. At these sites, frost heave as measured at the rail surface may reach nearly 20 mm, which is a significant threat to operations. The climate of Northeast China, strongly influenced by Mongolian–Siberian high pressure, features winters lasting 5–6 months with air temperatures reaching below –30 °C. Summers, under the influence of the southeast monsoon, are marked by heavy rainfall, while winters experience frequent snowfall and long accumulation periods [6]. As of February 2025, the region has 23 high-speed railway lines either operating or under construction, totaling approximately 5,100 km. Frost-induced subgrade defects are widespread, and on some lines, such as the Harbin–Dalian high-speed railway, winter speed restrictions are common [7,8]. Thus, preventing frost-heave damage during the service phase

remains a pressing challenge.

Current maintenance relies mainly on indirect measures such as fastener adjustment or rail pad insertion/removal to restore track smoothness. Once frost damage exceeds allowable limits, however, direct remediation becomes necessary. Soil stabilization using cement, lime, or other additives can reduce the frost susceptibility of fills [9-11], but such measures are impractical after misalignments have arisen during operation. In terms of water control, capillary drainage structures have been developed [12], yet subgrades remain exposed to precipitation and surface infiltration. Because water and fine soil fractions are invariably present, frost heave remains an inherent risk in coarse-grained fills [13,14].

Temperature-based countermeasures include thermal insulation layers, slope protection, and insulation berms [15–17]. However, installing insulation layers in the upper subgrade requires ballast removal and subgrade cutting, leading to high costs [18,19]. Further, in the event of heavy precipitation, the presence of shallow groundwater, strong cold waves, and rapid temperature drops make frost damage difficult to eliminate. Therefore it often reoccurs.

In recent years, transportation infrastructure agencies have developed a range of electrified, active temperature-control technologies [20–22]. These approaches embed heating elements into structures to increase temperature through active heat input. Applications now include energy pavements, energy tunnels, energy piles, and energy diaphragm walls. For pavements, active snow-melting systems employing electric heating materials (graphene, carbon fibers, stainless-steel wires) have been

implemented on bridge decks, roadways, and airport runways [23–25]. Renewable-energy-driven systems based on solar or geothermal sources have also been tested, raising pavement temperatures by 15–20 °C [26-28]. Similar heating methods have been deployed in underground structures, tunnel linings, and retaining walls, supported by standards such as ASHRAE guidelines, DB42T 1503-2019, and JGJ/T 438-2018 [29–33].

The railway sector has likewise promoted active temperature-control technologies. For example, turnout snow-melting systems have been standardized (TB/T 3539-2018), and solar-driven refrigeration devices have been trialed for permafrost stabilization [34]. For subgrades, proposed strategies include electric heating rods [35], solar vacuum heat collectors [36,37], and ground-source heat pump systems with distributed exchangers [38,39]. These solutions have shown promise in general-speed railways with ballasted track, but their application to high-speed railways with ballastless track remains untested.

To address this gap, we constructed a test section (DK413+80–DK413+100) on the Shenyang–Baishan high-speed railway incorporating a ground-source heat pump (GSHP) active heating system. A field experiment was conducted during the 2024–2025 winter to evaluate its effectiveness in mitigating frost heave.

2. General Design Considerations for a Geothermal Heat Pump System for Frost Heave Prevention

A heat pump is a high-efficiency energy device that extracts low-grade thermal energy from the environment and upgrades it for heating. Its core components include

a compressor, two heat exchangers (evaporator and condenser), and a throttle valve. Following the reverse Carnot cycle, the refrigerant undergoes evaporation at low temperature and pressure, absorbs ambient heat, and transforms into a low-pressure gas. This gas is compressed to raise its pressure and temperature, then condensed to release latent heat, returning it to the liquid state. After throttling, the refrigerant reverts to a low-pressure liquid, completing the closed cycle of heat collection, conversion, and release.

Heat pumps offer two main advantages. First, they have a broad operating temperature range: evaporator cooling can reach as low as –40 °C, while condenser heating can exceed 90 °C, enabling operation in both extreme cold and hot conditions. Second, their coefficient of performance (COP) typically ranges from 3 to 5, meaning that 1 unit of input energy can deliver 3–5 units of heat. As a result, heat pumps are widely applied in residential and industrial heating and cooling, including air-source, water-source, ground-source, and multisource composite systems. Their efficiency and adaptability make them suitable for frost-heave prevention in traffic subgrades exposed to cold climates.

However, transportation subgrades are typically long and exposed, with frost-heave zones distributed over large distances. Large centralized heat pump units, while powerful, are poorly matched to subgrade heat demand: long-distance refrigerant piping incurs conductive and convective heat losses and results in pressure drop losses, reducing system efficiency. To overcome this mismatch, a dedicated subgrade-oriented GSHP system was designed (Fig. 1). Unlike conventional refrigerant–water secondary

systems, this scheme adopts direct-expansion heat exchange, in which refrigerant pipelines are buried directly in soil. This eliminates intermediate heat-transfer losses and pump energy consumption, shortening the heat transfer chain. Each surface unit integrates a compressor, throttle, and monitoring/control components within a compact enclosure.

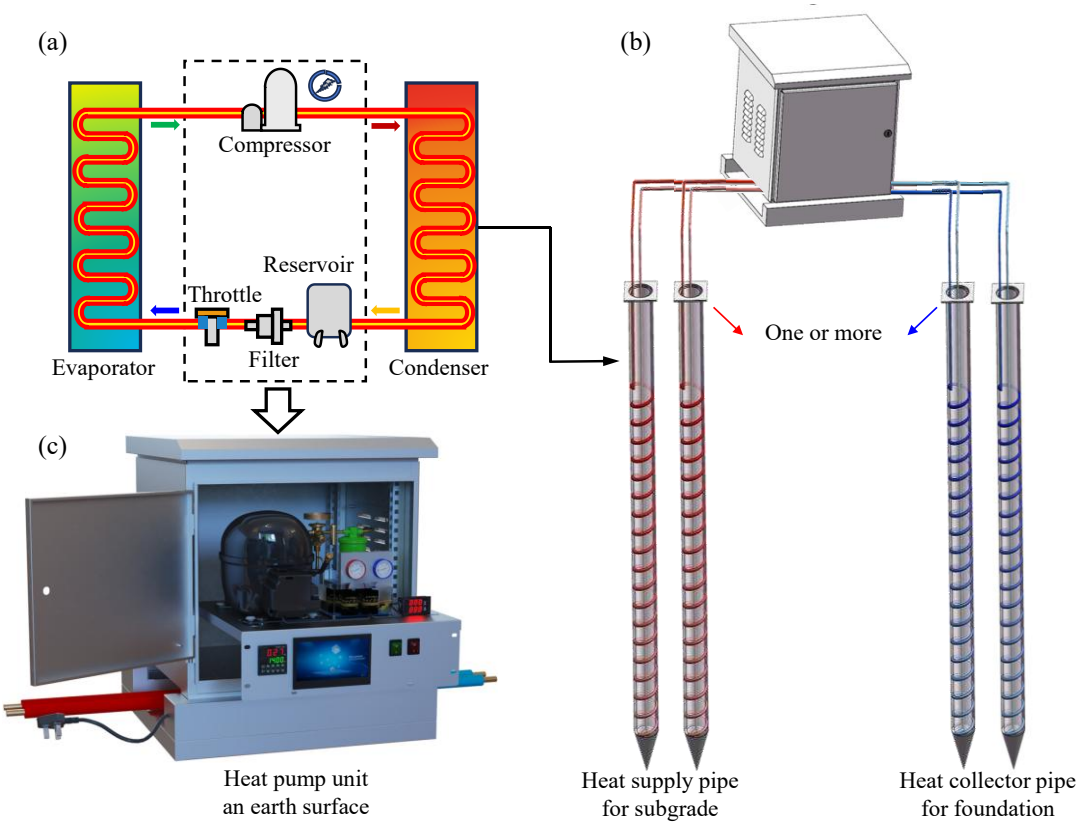

Fig. 1. Ground-source heat pump system for railway subgrades: (a) schematic of the direct-expansion refrigeration cycle; (b) surface unit connected to vertical ground heat collectors (supply/red, return/blue); (c) opened surface unit showing compressor and control components.

When selecting heat sources, geothermal, solar, and air energy are viable options. In this study, shallow geothermal energy was chosen for its stability, abundance, and ease of use. Near-surface geothermal resources are stratified: the top 10 m is usually

considered the temperature-varying layer which is affected by seasonal climate, while the layer at 10–20 m depth is the constant-temperature zone at the regional mean air temperature. Below this lies the warming zone controlled by the Earth's geothermal gradient. The shallow layers are characterized by rapid energy recovery, reliable reserves, and no depletion risks, making them suitable for long-term operation.

The GSHP application scheme for subgrades is shown in Fig. 2. Vertically buried heat collector pipes (evaporators) are placed in the foundation adjacent to the embankment, while heat-supply pipes (condensers) are horizontally embedded in frost-susceptible subgrade zones. Surface-mounted heat pump units provide compression and circulation. In the longitudinal direction, a distributed layout is adopted, with systems evenly arranged along frost-prone sections. This distributed design ensures localized heat supply aligned with the thermal demand of subgrades common in cold regions.

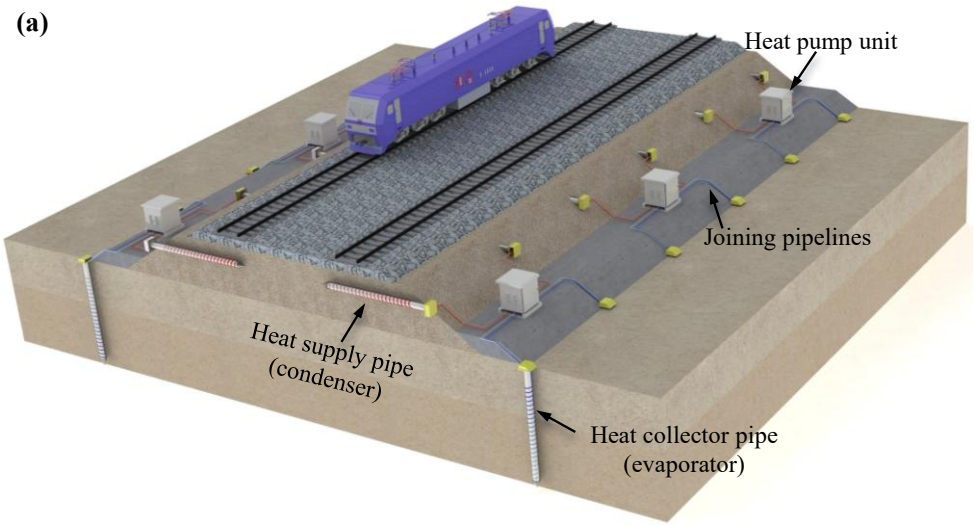

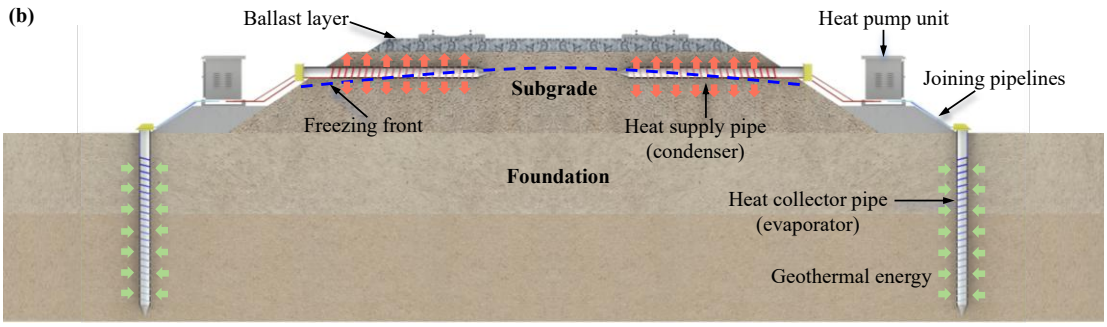

Fig. 2. Distributed arrangement of the ground-source heat pumps: (a) 3D schematic diagram illustrating vertical collectors and horizontal supply pipes; (b) cross-sectional arrangement within the subgrade.

3. Field deployment on a High-Speed Railway

To validate the effectiveness of the proposed GSHP system under realistic conditions, a full-scale test was conducted on the Shenyang–Baishan high-speed railway in Northeast China. This section introduces the site conditions, climatic features, thermal demand analysis, and the design and construction of the experimental test section. The detailed instrumentation and monitoring program are also described.

3.1 Environmental conditions and design scheme

The Shenyang–Baishan high-speed railway, a section of the Shenyang–Jiamusi corridor, was designed for a maximum linespeed of 350 km/h. The total project length is 430.1 km, oriented east–west across the northeastern part of Liaoning Province and the southeastern part of Jilin Province (Fig. 3a).

The test site is located in the Changbai Mountain region, which experiences a temperate continental monsoon climate with large seasonal variability. The mean annual temperature is approximately 1.7 °C, while the historical extreme minimum can fall to –40 °C. The maximum recorded temperature range reaches 70.4 °C. The

maximum frost depth is 1.98 m, while the design frost depth is 2.4 m. The average temperature in January can drop to –10 °C, and more than eight cold-wave events occur annually. Annual precipitation is approximately 1,000 mm, with snowfall contributing about 500 mm. It is common for snow accumulation on the ground to reach ≈2.0 m depth. The area belongs to the Songhua River catchment with dense surface drainage and abundant groundwater, thus providing highly frost-susceptible subgrade conditions.

The DK413+50–DK413+100 section (128°E, 42.5°N) was selected as the field test site (Fig. 3b). The railway alignment passes through mountainous valleys and forested areas, where groundwater convergence and water exposure conditions are significant. The test section is composed of a dual-line embankment structure with a 5 m track spacing, 13.6 m top width, and 4.3 m slope height. The trackbed consists of a composite, layered structure (Figure 3c):

1. Surface layer: 0.4 m thick graded gravel with 3% cement to improving freeze–thaw resistance;
2. Frost-heave-resistant layer: a 1.8 m thick layer (Group A/B soil) and a transition layer 0.5 m thick (Group A/B soil);
3. Main body layer: a 1.1 m thick layer (Group A/B/C soil with ≥30% sand for drainage);
4. Gravel cushion: a 0.5 m thick layer with 20–40 mm particles, to block the capillary rise of water.

Earthwork construction began in July 2023 and was completed in May 2024. Compaction was controlled between 93% and 97%.

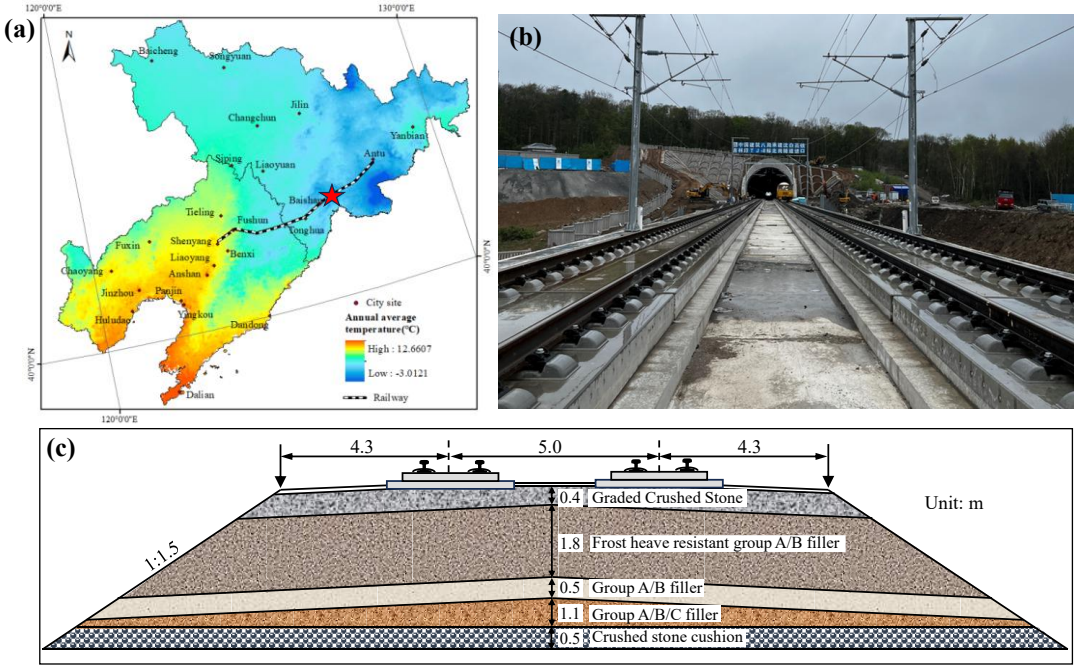

Fig. 3. Location and design of the field test section on the Shenyang–Baishan HSR: (a) geographical context; (b) full view of the test site; (c) cross-sectional structure of the layered subgrade.

3.2 Meteorological conditions and frost-heave potential

The winter season in the Changbai Mountains typically extends from early October to the end of March. The air temperature records from 2023 to 2024 exhibited three stages: a decreasing stage, a sustained low-temperature stage, and a rising stage (Fig. 4a).

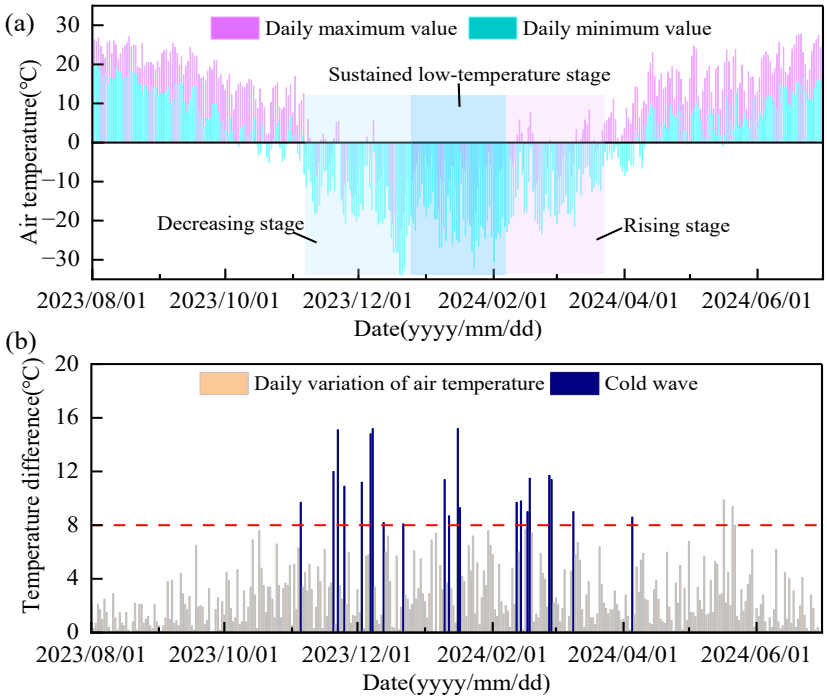

202

203 **Fig. 4.** Meteorological conditions at the test site: (a) seasonal air temperature evolution;

204 (b) frequency and intensity of cold-wave events.

205 Cold-wave events were frequent and intense. The maximum daily air temperature

206 drop was 15.2 °C, and the absolute minimum reached –34 °C. The monthly mean

207 temperature in January was –14.3 °C. Cold waves were classified into three categories:

208 Mild: –4 to –6 °C daily decrease; Moderate: –6 to –8 °C daily decrease; Severe: < –

209 8 °C daily decrease.

210 As shown in Fig. 4b, severe cooling occurred 8 times during the decreasing stage

211 (mid-November to early December 2023), 5 times during the sustained stage (late

212 December to mid-January), and 7 times during the warming stage (early February to

213 early March 2024). Thus, compared to other cold regions of Northeast China, the

214 Changbai Mountain area experiences high-frequency, high-intensity severe cooling.

215 Precipitation further aggravates frost risk. During autumn-to-early-winter

transitions and post-snowmelt, the subgrade moisture content is high. Severe cold-wave events interacting with water-saturated soil layers cause rapid frost propagation and frost heave under steep temperature gradients, differing from the slower freezing processes of milder regions.

3.3 Heat load analysis

To quantify thermal demand, the DeST building thermal environment toolkit [40] was employed. The subgrade was analogized to a building, discretized into microelements, and modeled dynamically. The DK413+100 cross-section was selected for calculation.

Fig. 5 shows that heat load demand began in early November and lasted until mid-April. The daily mean heat load peaked on January 12, about 7 days later than the coldest day (January 5), reflecting the soil's thermal inertia. Over the freezing period, the maximum heat load reached 1,183 W/linear meter, while the mean load was 596 W/linear meter.

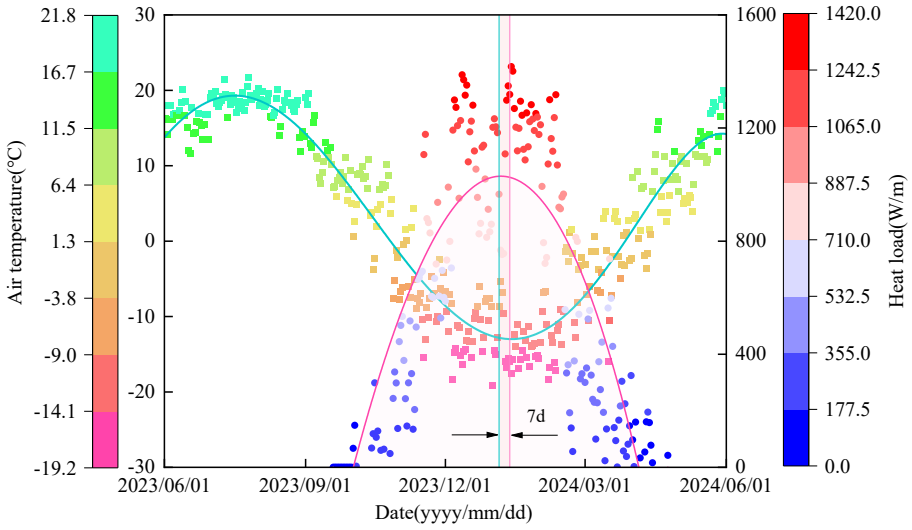

Fig. 5. Time series of daily heat load demand for the test subgrade, showing the relationship with air temperature.

The depth distribution is shown in Fig. 6. Heat demand decreases with depth, consistent with the geothermal gradient. More than 65% of the total heat load is concentrated within the near-surface frozen zone. At 1 January, the surface-layer demand reached 1,022 W/m, or ≈78% of the total. The heat demand below 1.5 m was minimal (≈13 W/m). These results confirm that shallow frost control is critical, and design should focus on mitigating heat loss in the upper subgrade.

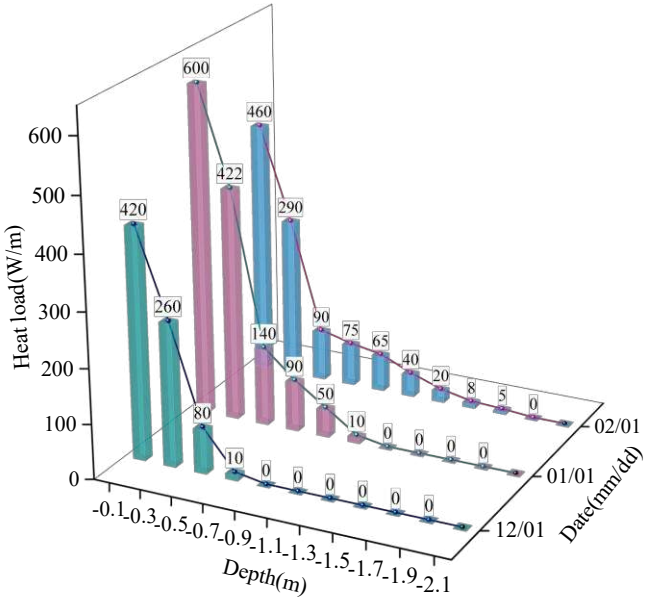

Fig. 6. Depth distribution of calculated heat load, highlighting concentration of demand within the frost-susceptible upper layers.

3.4 Heat pump design and monitoring scheme

A GSHP test section was constructed on the up-track between DK413+80 and DK413+100 (Fig. 7). Ten heat pump units were evenly distributed across 20 m, with a longitudinal spacing of 2.0 m. Each heat-supply pipe (HS1–HS10) was 6.0 m long and 114 mm in diameter, and was buried horizontally at a depth of 95 cm below the subgrade surface, corresponding to 55 cm beneath the bottom of the surface layer. Each heat-collector pipe (HC1–HC10) was 6.0 m long and 114 mm in diameter, and was vertically

installed 5 m outside the slope toe.

The GSHP units were integrated within protective boxes measuring 0.5 × 0.5 × 0.5 m. Each box housed two compressors, throttles, and monitoring/control units, and was mounted on a concrete platform 0.5 m from the slope toe. Considering that the mean subgrade heat load during the freezing period was 596 W/linear meter, the rated output of each pump was designed to be 1200 W, thereby meeting the expected heating demand.

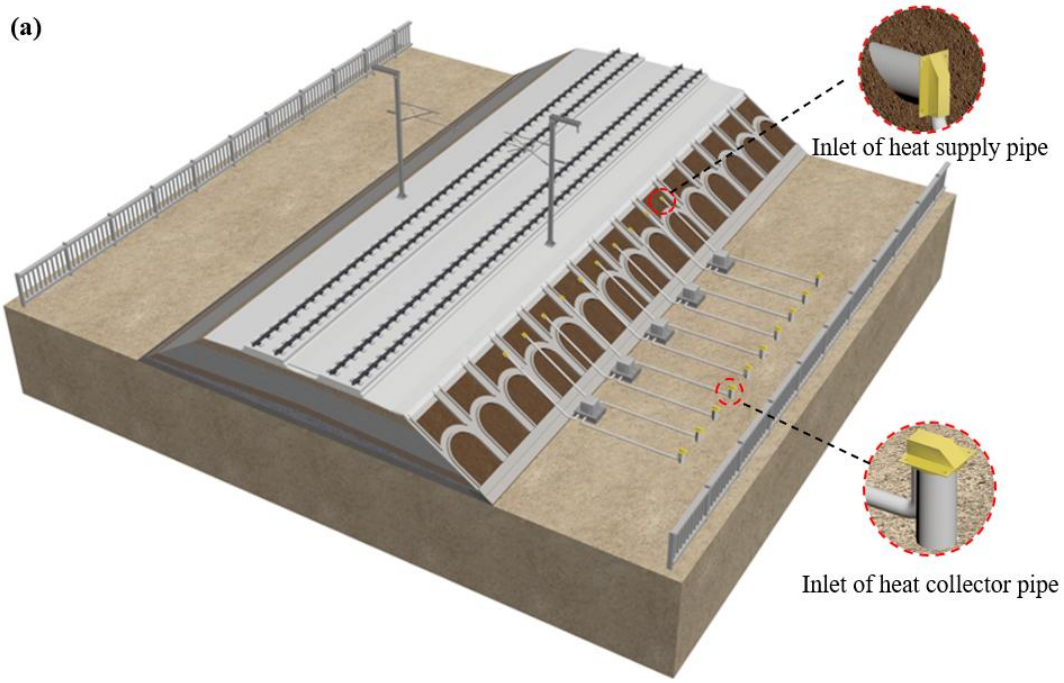

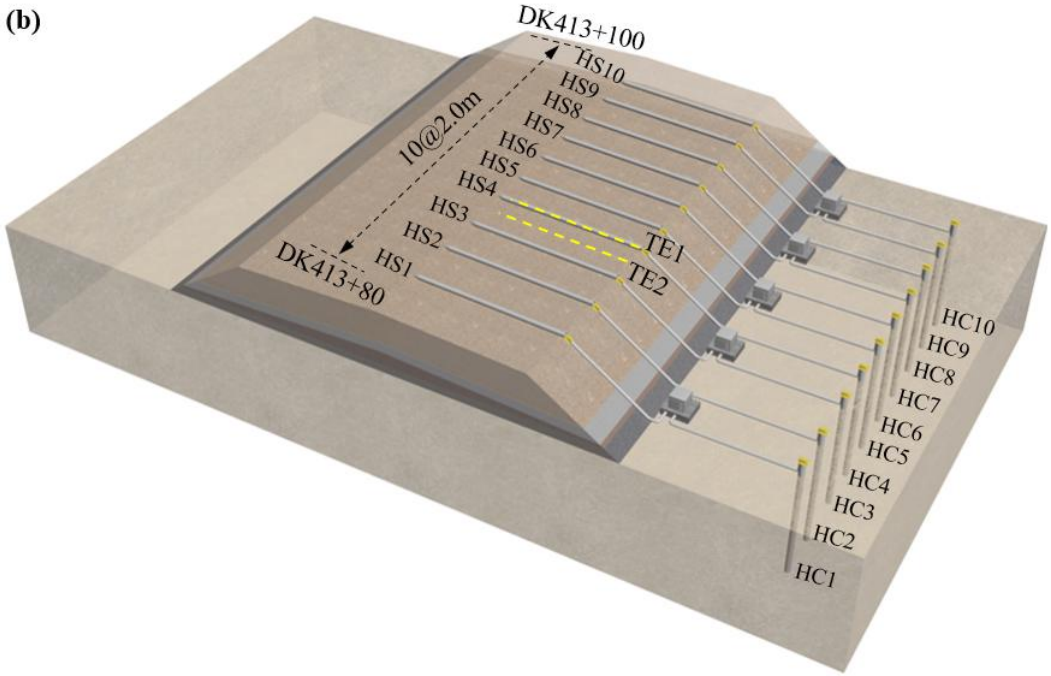

Fig. 7. Test section equipped with ground-source heat pumps: (a) field installation; (b) schematic of longitudinal and transverse layout.

Monitoring covered both the operating performance of the heat pump system and the thermal response of the subgrade (Fig. 8). For the pumps, three thermistors were installed at the inlet, midpoint, and outlet of both the heat-supply and heat-collector pipes, labeled TS1-1 to TS1-3 and TC1-1 to TC1-3, respectively. For the subgrade, three instrumented cross-sections and one longitudinal section were arranged. Cross-section TE1 was located at HS4 (DK413+87), TE2 was placed midway between HS3 and HS4 (DK413+86), and TE3 represented the untreated control subgrade 20 m away at DK413+60. At each cross-section, four temperature sensor chains were embedded: chains I and II were 6.0 m long and buried at depths of 50 cm and 75 cm, with five evenly spaced sensors at 1.5 m intervals; chains III and IV were 8.0 m long and buried at depths of 145 cm and 245 cm, with five sensors spaced at 2.0 m intervals. The sensors were numbered: A1–A4 for TE1, B1–B4 for TE2, and C1–C4 for TE3.

In addition, a longitudinal section (TE4) was arranged between HS3 and HS4 at a lateral distance of 3.0 m from the slope toe. Ten thermistors (D1–D10) were buried at a vertical depth of 95 cm, corresponding to the burial depth of the heat-supply pipes, and were evenly spaced at 20 cm intervals. All sensors were high-precision thermistors with an accuracy of ±0.05 °C. Data were recorded automatically at 15 min intervals and transmitted wirelessly for storage and analysis.

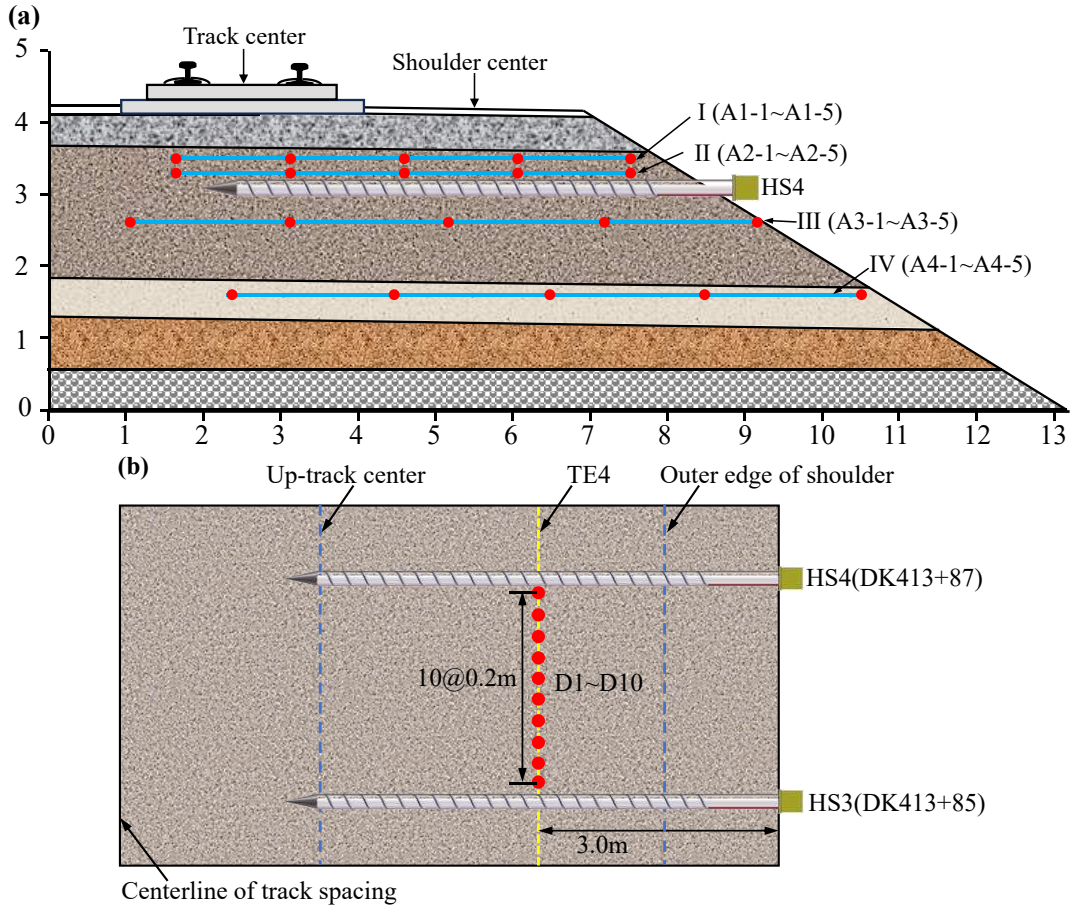

Fig. 8. Monitoring instrumentation plan: (a) cross-section at DK413+87 (TE1); (b) horizontal section at burial depth of 0.95 m.

3.5 Subgrade construction and monitoring in the test section

Subgrade construction began in September 2023. When the fill reached the target depth (55 cm below the surface layer), horizontal trenches (6 m × 20 cm × 20 cm) were

285 excavated to install conduits for the heat-supply pipes. Stainless steel conduits were
286 laid, aligned, and backfilled with fine sand to protect against collapse (Fig. 9a–c).
287 Trenches were then layered with frost-resistant soil for compaction.

288 At the slope toe, a geological drilling rig excavated ten vertical holes (6 m depth,
289 150 mm diameter, at 2 m spacing). Stainless steel conduits were inserted and backfilled
290 with fine sand to improve heat exchange. After the base layers were complete in
291 October 2023, surcharge preloading was performed. The surface layer was deferred
292 until April 2024 (Fig. 9d), after which the prefabricated heat-supply and collector pipes
293 were inserted into the conduits and filled with diathermic fluid to enhance thermal
294 transfer (Fig. 9e–f). Five protective cabinets housing dual-pump systems were installed
295 at 4 m spacing along the line, connecting heat pumps to the supply and collector pipes
296 (Figure 9g–h). Subgrade filling and system installation was finished in May 2024
297 (Figure 9i).

Fig. 9. Construction of the test section: (a–c) trench excavation and pipe installation; (d) surface layer placement; (e–f) pipe insertion; (g–h) installation of protective cabinets with pump units; (i) completed system.

Monitoring ran from May 2024 to May 2025. Based on optimization of the start–stop ratio and heat load calculations, the pumps were operated intermittently at '2.5 h on : 0.5 h off'. The heating period spanned January 7 to March 3, 2025, corresponding to the coldest phase of winter in the lunar calendar.

4. Thermal Regime and Frost Heave of the Common Subgrade

Before evaluating the impact of active heating, it is necessary to establish a baseline of frost action in an untreated subgrade under the same environmental conditions. Thus, this section presents the observed soil temperature evolution, frost depth development and track deformation in the control section, thereby providing a

311 benchmark for comparison with the heated test section.

312 ### 4.1 Soil temperature variation

313 Fig. 10 shows the evolution of soil temperature in the untreated subgrade (cross-
314 section TE3) at depths of 50, 75, 145, and 245 cm between November 1, 2024, and
315 April 1, 2025. The overall process can be divided into three distinct stages: rapid
316 decrease, gradual decrease, and recovery.

317 During the rapid decrease stage (early November to mid-December), cooling
318 proceeded quickly as air temperature dropped. At 50 cm depth, sensors C1-1 to C1-5
319 recorded cooling rates of ≈0.43–1.68 °C/d. At 75 cm depth (C2-1 to C2-5), the rates
320 were lower, ≈0.19–0.22 °C/d. By December 15, the soil in the shoulder had cooled by
321 10.68 °C, compared with 8.66 °C at the track center, indicating that the shoulder
322 experienced more rapid thermal exchange due to its greater exposure.

323 During the gradually decreasing stage (mid-December to early March), cooling
324 slowed across all depths. However, temperatures near the slope surface still fluctuated
325 synchronously with the air temperature, reflecting continued atmospheric influence.
326 The minimum soil temperatures occurred between late February and early March. At
327 50 cm depth, minima of –8.84 °C at the shoulder center and –3.77 °C at the track center
328 were recorded. At 75 cm, the minimum values were –7.95 °C (shoulder center) and –
329 3.25 °C (track center). At greater depths, the minimums were –5.60 °C and –1.48 °C at
330 145 cm, and –3.13 °C and +2.31 °C at 245 cm, respectively. These data confirmed that
331 the shoulder zone cooled more rapidly and reached lower temperatures than the track
332 center.

During the recovery stage (late March to April), soil temperatures at all depths began to rise with increasing air temperature. Warming progressed from the surface downward, with upper layers responding first and deeper layers lagging behind. Horizontally, warming was faster near the shoulder, where external heating and lateral thawing accelerated the process. Once the thaw fronts moving downward from the surface and upward from the depth intersected, the seasonal freeze–thaw cycle ended.

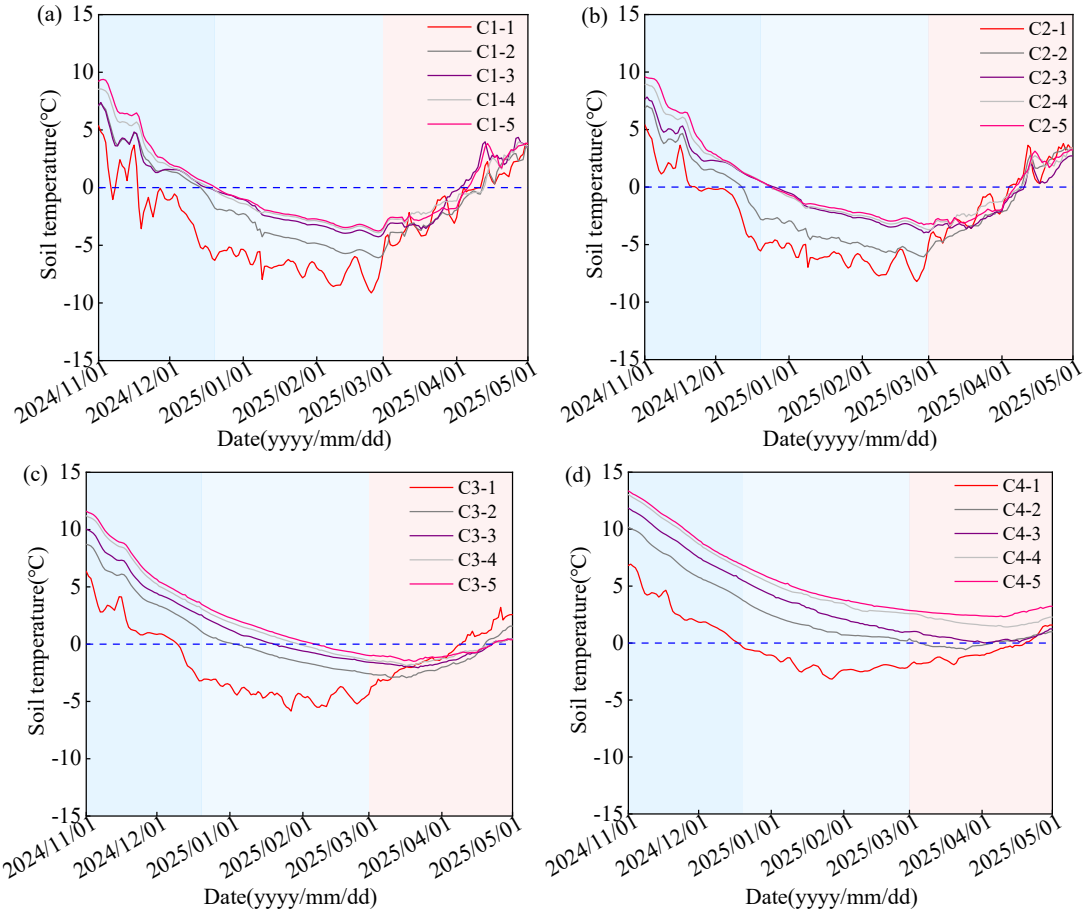

Fig. 10. Soil temperature evolution in the untreated subgrade (TE3) at depths of (a) 50, (b) 75, (c) 145, and (d) 245 cm.

Fig. 11 provides spatial snapshots of the temperature field. At the beginning of freezing (January 5), the soil temperature at 10 cm depth was ≈ –4 °C, with frost depths of 103 cm at the track center and 126 cm at the shoulder center. By February 10, the

temperature at 10 cm depth had dropped to ≈ –8 °C, while frost penetration deepened further. By March 3, frost depths reached 174 cm (track center) and 199 cm (shoulder center), highlighting the greater vulnerability of the shoulder to cold penetration.

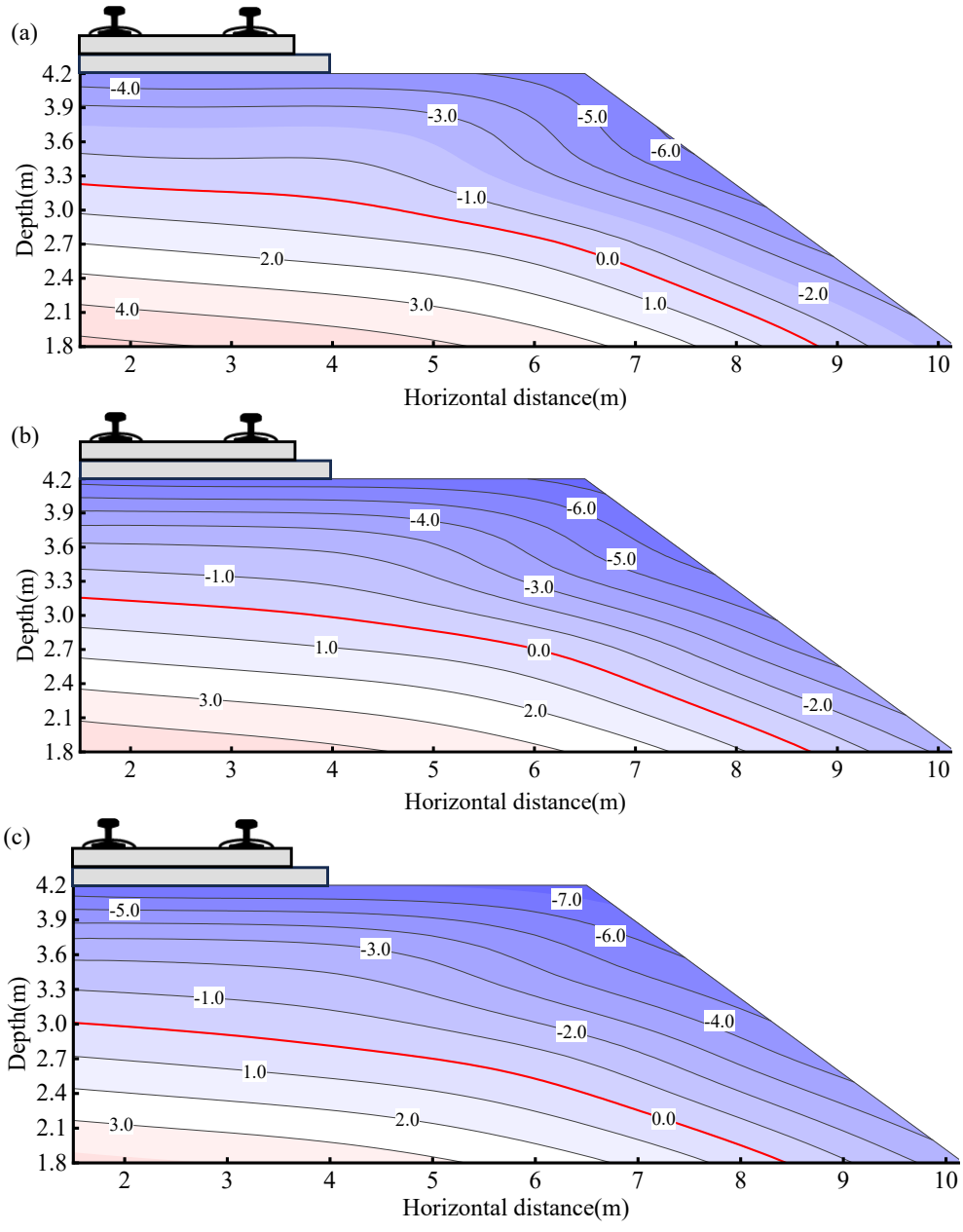

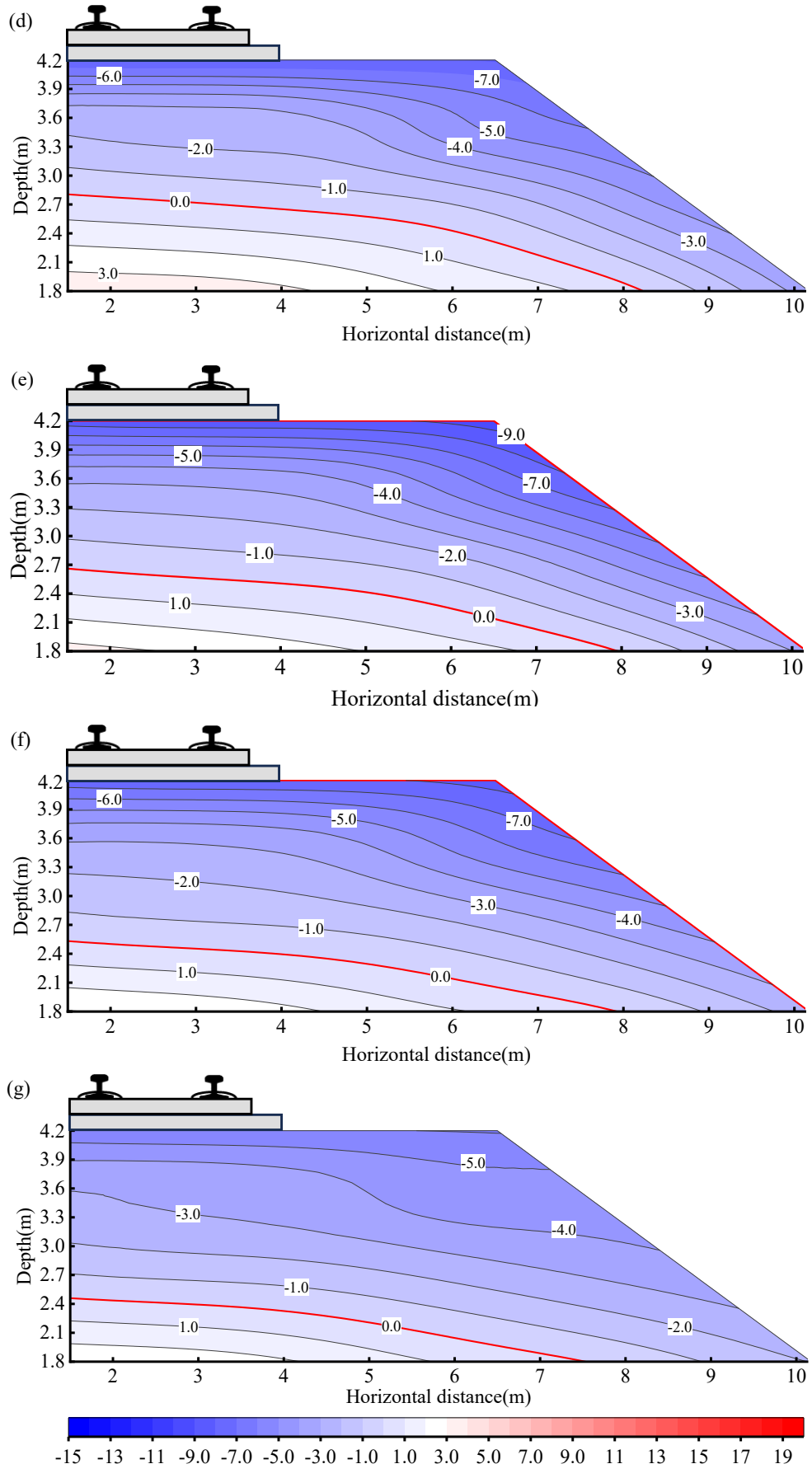

Fig. 11. Snapshots of soil temperature fields in the untreated subgrade (TE3) at different

357 winter stages: (a) January 5, 2025; (b) January 10, 2025; (c) January 20, 2025; (d)
358 January 30, 2025; (f) February 20, 2025; (g) March 3, 2025.

359 ### 4.2 Frost depth development

360 The temporal progression of frost depth in the untreated subgrade is shown in Fig.
361 12. At the onset of freezing, the frost front propagated steadily downward in both the
362 track center and shoulder. The average advancement rates were ≈1.4–1.7 cm/d, with
363 daily maxima of 3.9 cm/d at the track center and 4.2 cm/d at the shoulder. The faster
364 shoulder progression reflects its higher exposure to cold air on multiple sides.

365 By late March, maximum frost depths had been reached: ≈195 cm at the track
366 center and ≈224 cm at the shoulder center. Thus, these values exceeded the design frost
367 depth of 2.0 m, confirming the severe freezing environment of the Changbai Mountain
368 area. After early April, upward thawing began. The turning point occurred on April 3 at
369 the track center and on April 6 at the shoulder, when frost fronts reversed direction. By
370 April 9–10, both locations showed bidirectional thawing, with melting progressing
371 from both the surface and depth toward the mid-layer.

372 Because of snow cover, surface thawing lagged behind the upward migration of
373 the frost front. Once surface thaw initiated, the thaw duration was short compared with
374 freezing. The total frost duration was ≈153 days at the track center and ≈158 days at the
375 shoulder. In contrast, thawing lasted only ≈9 days at the track center and ≈13 days at
376 the shoulder. This asymmetry demonstrates the difficulty of frost control in this climate,
377 where prolonged freezing dominates over a much shorter thawing phase.

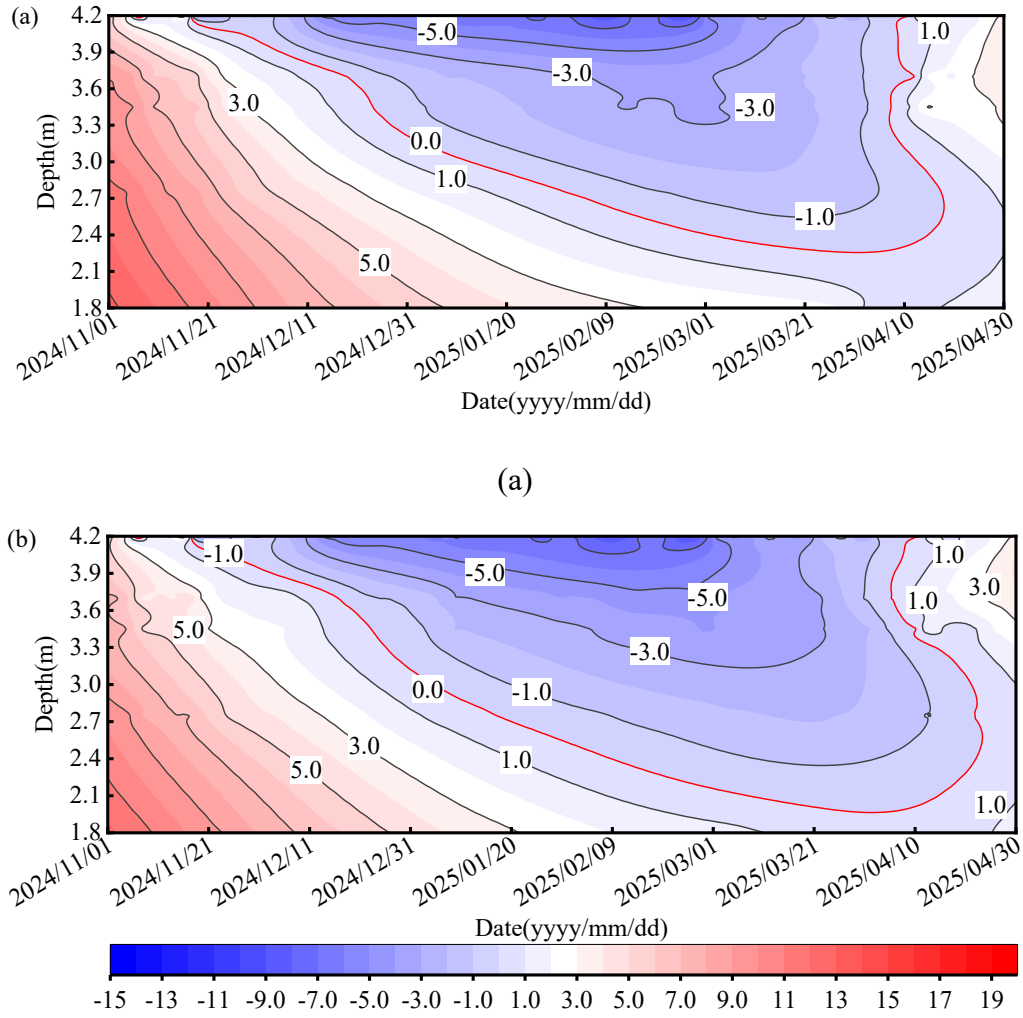

Fig. 12. Temporal development of frost depth in the untreated subgrade: (a) track center; (b) shoulder center.

4.3 Track surface deformation

Fig. 13 illustrates the frost-heave displacement of the untreated subgrade between November 2024 and April 2025. Prior to December, deformation remained within ±1 mm, reflecting negligible frost activity while air temperatures were still moderate. However, after December, the combined effects of sharp air temperature drops and snowmelt infiltration initiated significant frost heave.

As freezing progressed, track surface deformation increased continuously. By

mid-March, maximum frost heave reached ≈6.6 mm at the up-track center (DK413+160) and ≈5.2 mm at the down-track center. Both exceeded the frost-heave safety limit of 5 mm specified in the *Code for Design of Railway Subgrades*. These exceedances highlight the severity of frost-heave risk under natural conditions in this region.

The deformation pattern also displayed spatial variability. Shoulders generally experienced greater heave than the track center, consistent with their deeper frost penetration. Longitudinally, the amplitude varied between different monitoring points, reflecting heterogeneity in soil properties and water distribution.

With the onset of spring, rising air temperatures initiated thawing. The heaved track surface gradually subsided, though the deformation release lagged behind the temperature rise due to the persistence of residual frozen layers at depth. The cycle confirmed that untreated subgrades in this environment cannot reliably maintain track geometry within safe limits throughout winter operation.

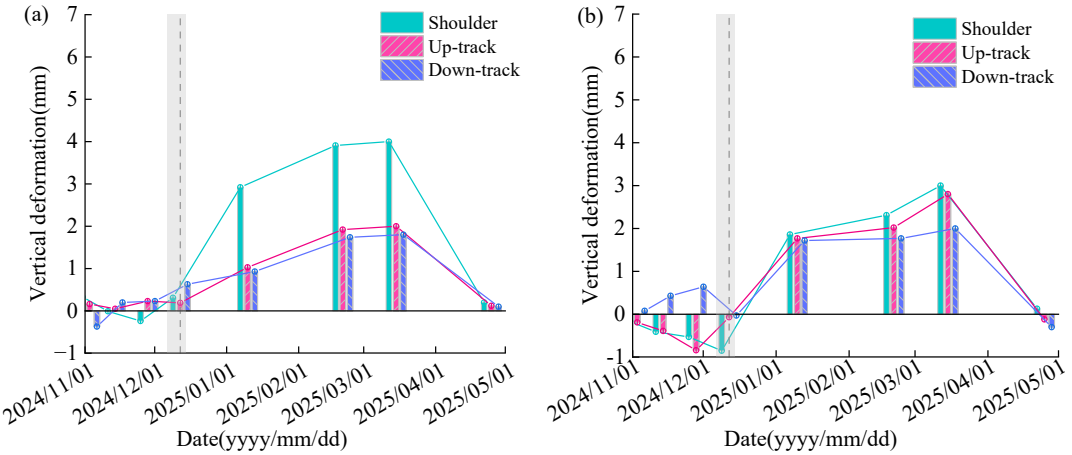

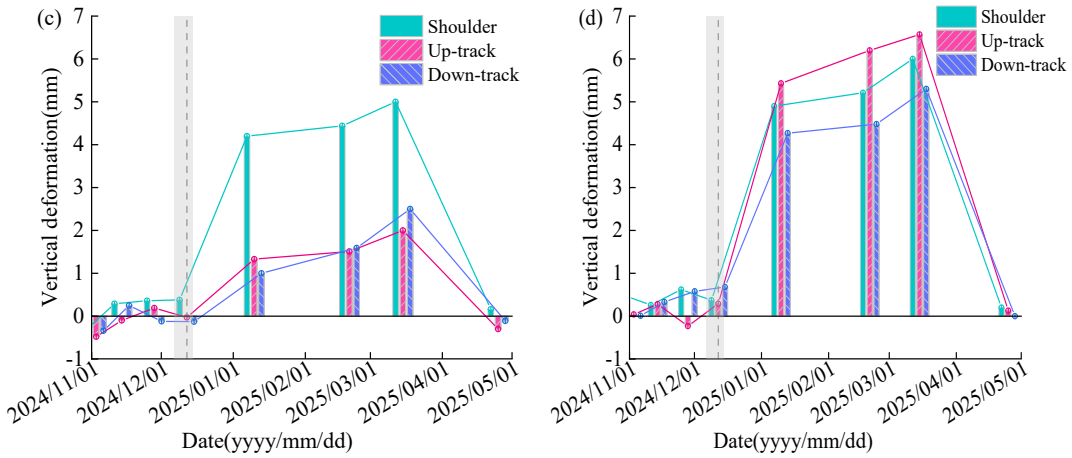

Fig. 13. Frost-heave displacement of the untreated track surface at selected monitoring points: (a) DK413+25; (b) DK413+60; (b) DK413+110; (d) DK413+160.

4.4 Heat pump operation performance

Fig. 14 presents the output temperature of the heat-supply pipes on February 1, 2025, during intermittent operational heating. At start-up, the inlet temperature (T1-1) increased at ≈2.02 °C/min, while the outlet (T1-3) rose at ≈1.12 °C/min, demonstrating rapid thermal responsiveness. Along the pipe, the outlet temperatures were consistently lower than the inlet values, confirming efficient heat delivery to the surrounding soil. The mid-pipe fluid temperature (TS1-2) remained stable within 16.0–21.0 °C, smoothing fluctuations and serving as a reliable heat source.

Daily output exhibited a minor diurnal pattern, with slightly higher efficiency between 11:00 and 16:00 due to solar radiation effects. However, the amplitude between the peak and trough was only ≈1.8 °C, indicating relatively stable performance.

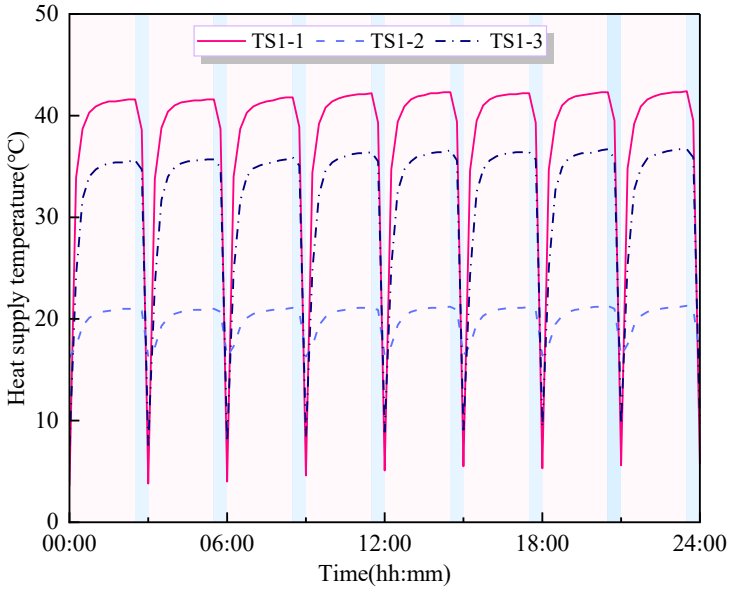

Fig. 14. Real-time outlet and inlet temperatures of heat-supply pipes during intermittent operation (2.5 h on : 0.5 h off).

Fig. 15 shows the long-term averages. After activation on January 8, the supply fluid temperature rose from ≈0 °C to 17.8 °C within four days (≈3.56 °C/d). Throughout the heating season, the fluid maintained an average of 18.7 °C, with a minima of 15.7 °C and a maxima of 22.2 °C. On January 18, the maximum outlet temperature reached 37.6 °C, while the return was 24.8 °C, giving a gradient of 12.8 °C. Over the entire period, the inlet–outlet difference remained ≈7.8–14.3 °C, confirming consistent heat transfer to the subgrade.

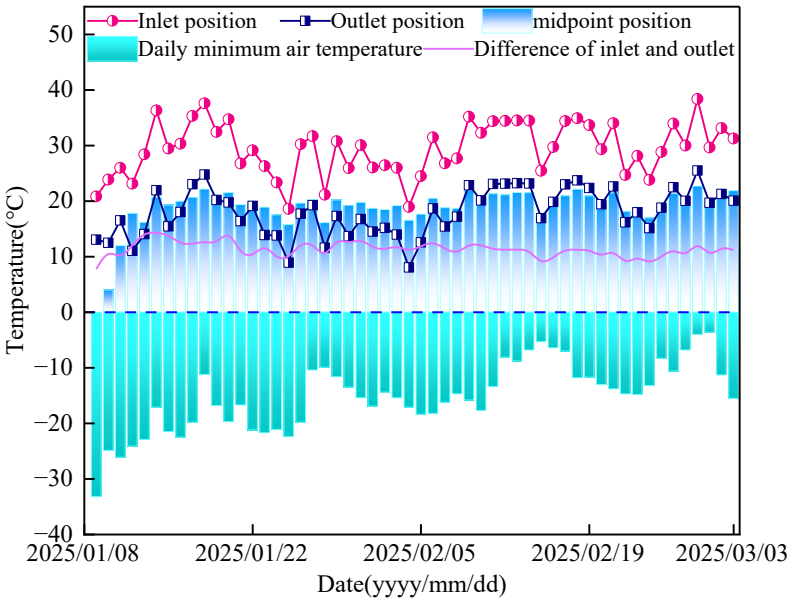

Fig. 15. Daily average outlet temperatures of heat-supply pipes during the heating season.

5. Thermal Regime and Frost Heave of the Heated Test Section

The thermal and deformation responses of the GSHP-equipped subgrade were analyzed to assess the mitigation performance of active heating. Results from the directly heated zones, intermediate areas between pipes, and longitudinal profiles are presented, thus offering a comprehensive evaluation of the spatial and temporal effects of geothermal heating on frost penetration and track stability.

5.1 Cross-section TE1 (with heat-supply pipe HS4)

Fig. 16 presents the soil temperature variation at TE1, where heat-supply pipe HS4 was embedded. Once the heat pumps began operation on January 7, 2025, the thermal regime at TE1 diverged significantly from that of the untreated subgrade. The strongest warming occurred in the upper layers closest to the pipe, while deeper layers experienced smaller and delayed temperature increases. For example, by January 30, the 50 cm depth sensors (A1-1 to A1-5) recorded temperatures of –1.22 to +0.17 °C,

445 whereas the corresponding untreated subgrade values at TE3 (C1-1 to C1-5) remained
446 between –6.95 and –2.73 °C. Thus, active heating raised the soil temperature by ≈1.5–
447 6.1 °C, in some cases shifting the soil from frozen to unfrozen conditions.

448 The spatial distribution of heating showed clear temperature gradients. At the same
449 depth, positions near the pipe inlet warmed more strongly than those closer to the outlet,
450 reflecting gradual attenuation along the flow path. On the slope surface, where
451 preheating minimums had been between –5.6 and –1.4 °C, soil temperatures by March
452 2 had risen to +0.9 to +4.8 °C, with only one position slightly below 0 °C (–0.7 °C).
453 These results indicate that the system reduced low-temperature extremes and, in many
454 locations, significantly mitigated frost-heave damage.

455
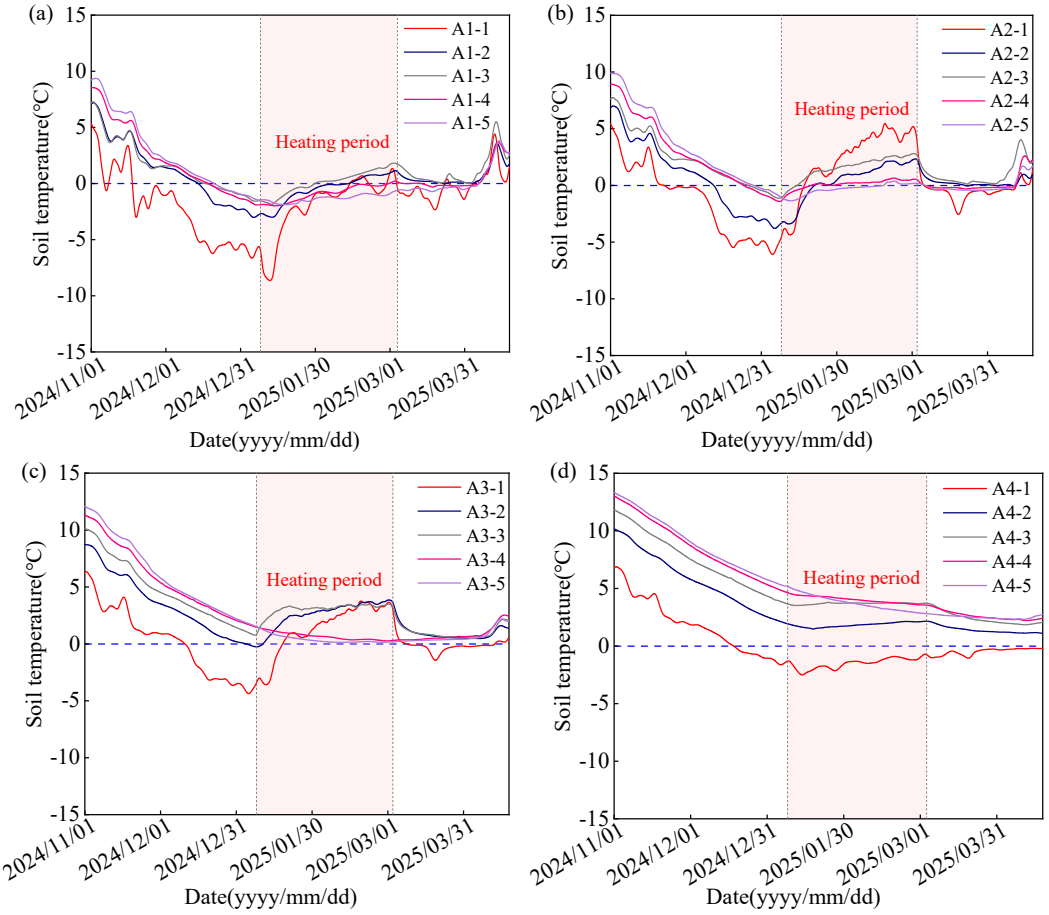

456

457 **Fig. 16.** Soil temperature variation at TE1 (with supply pipe HS4) at depths of (a) 50,

(b) 75, (c) 145, and (d) 245 cm.

Fig. 17 illustrates the resulting temperature field. Before heating, the subgrade exhibited a typical vertical thermal gradient with U-shaped isotherms and frost depths of 103 cm (track center) and 126 cm (shoulder center). Three days after heating commenced, an oval-shaped warm zone formed around the pipe, flattening isotherms and reducing frost depth to ≈90 cm. As heating continued, the minimum temperature at the bottom of the surface layer increased from –3.9 °C in the untreated subgrade to –2.4 °C at TE1. By March 3, frost penetration was restricted to 70 cm at the track center and 34 cm at the shoulder center, representing reductions of ≈104 cm and ≈165 cm relative to the control.

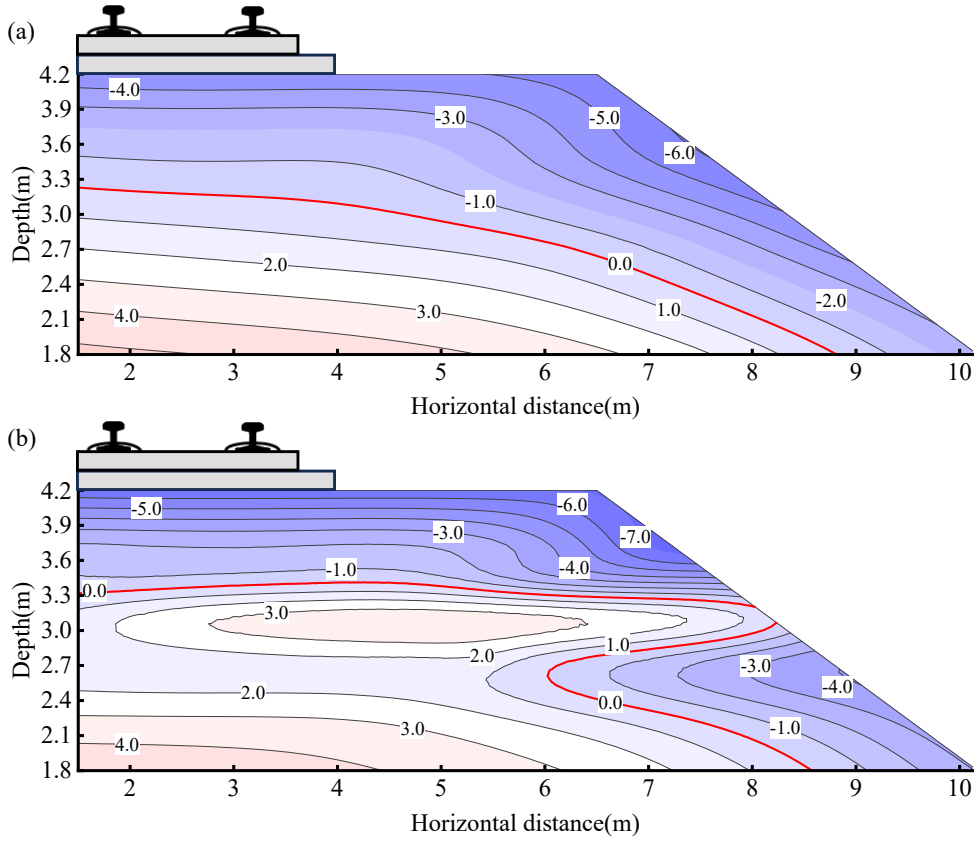

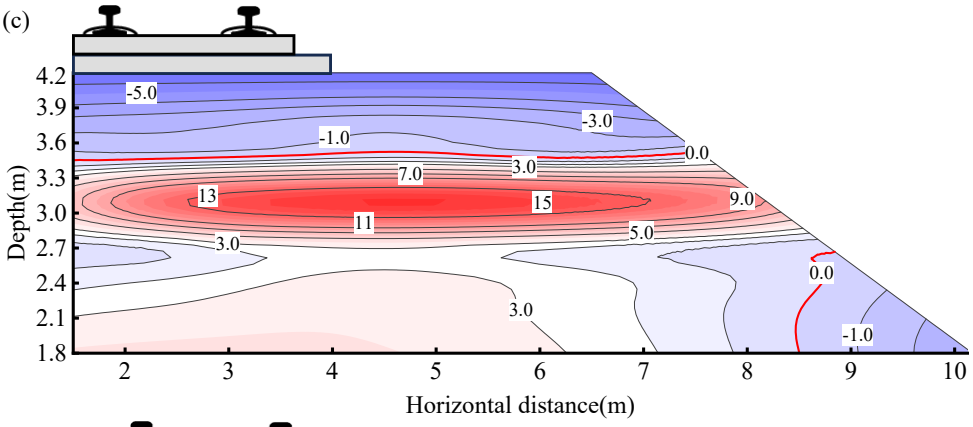

470

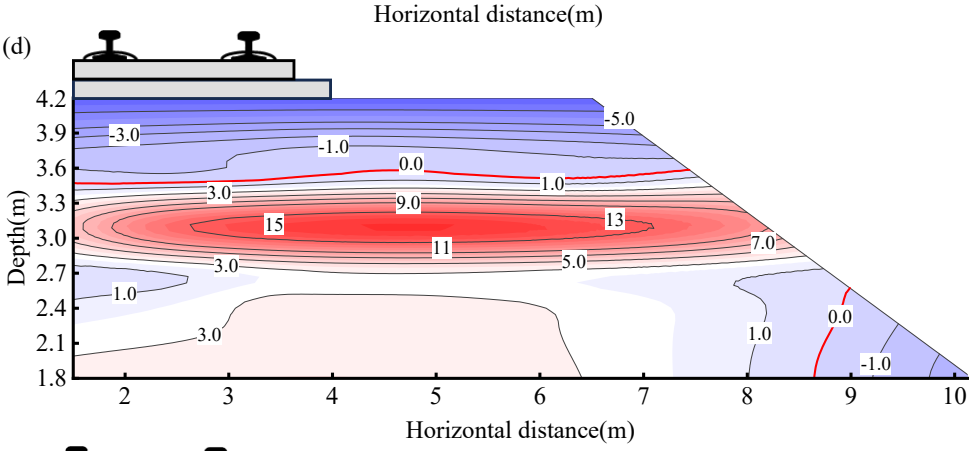

471

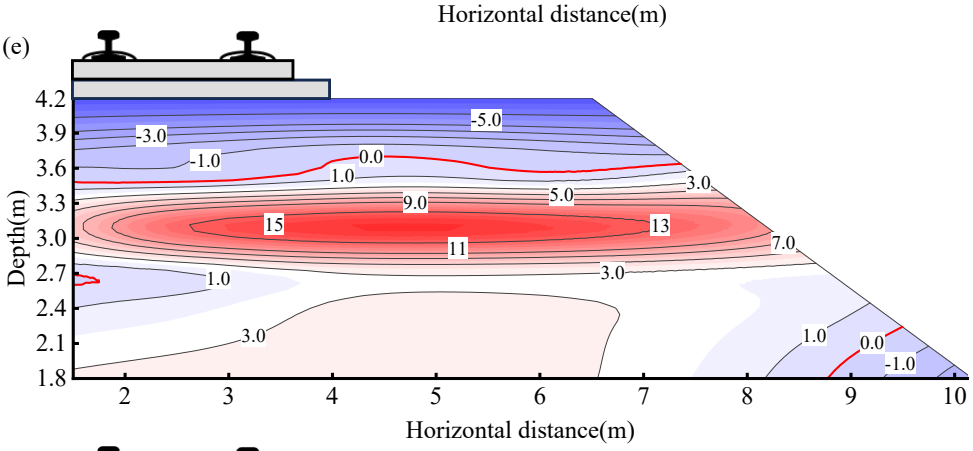

472

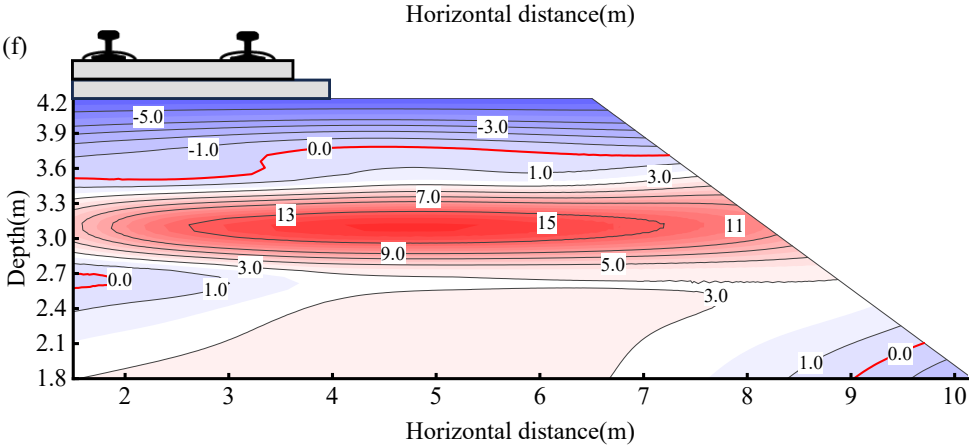

473

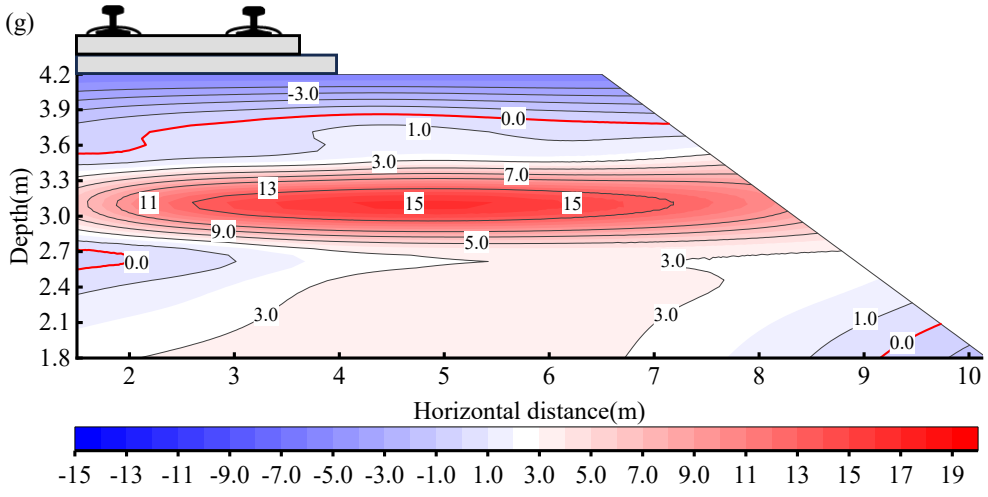

(g) March 3, 2025

Fig. 17. Thermal regime at TE1 before and after heating, showing development of the warm plume. (a) January 5, 2025; (b) January 10, 2025; (c) January 20, 2025; (d) January 30, 2025; (e) February 10, 2025; (f) February 20, 2025.

The frost depth time series (Fig. 18) confirms this process. Initially, frost depths at TE1 matched those at TE3, but following the heat pump activation they steadily decreased. Between January 7 and January 25, frost depth reduced at ≈1.6 cm/d at the track center and ≈2.7 cm/d at the shoulder, stabilizing thereafter at ≈78 and ≈66 cm, respectively. When spring arrived, the heated section thawed earlier than the untreated subgrade, completely melting ≈12 days sooner. Overall, heating not only restricted frost penetration but also accelerated the recovery of unfrozen conditions, with particularly strong benefits at the shoulder where natural frost penetration was deepest.

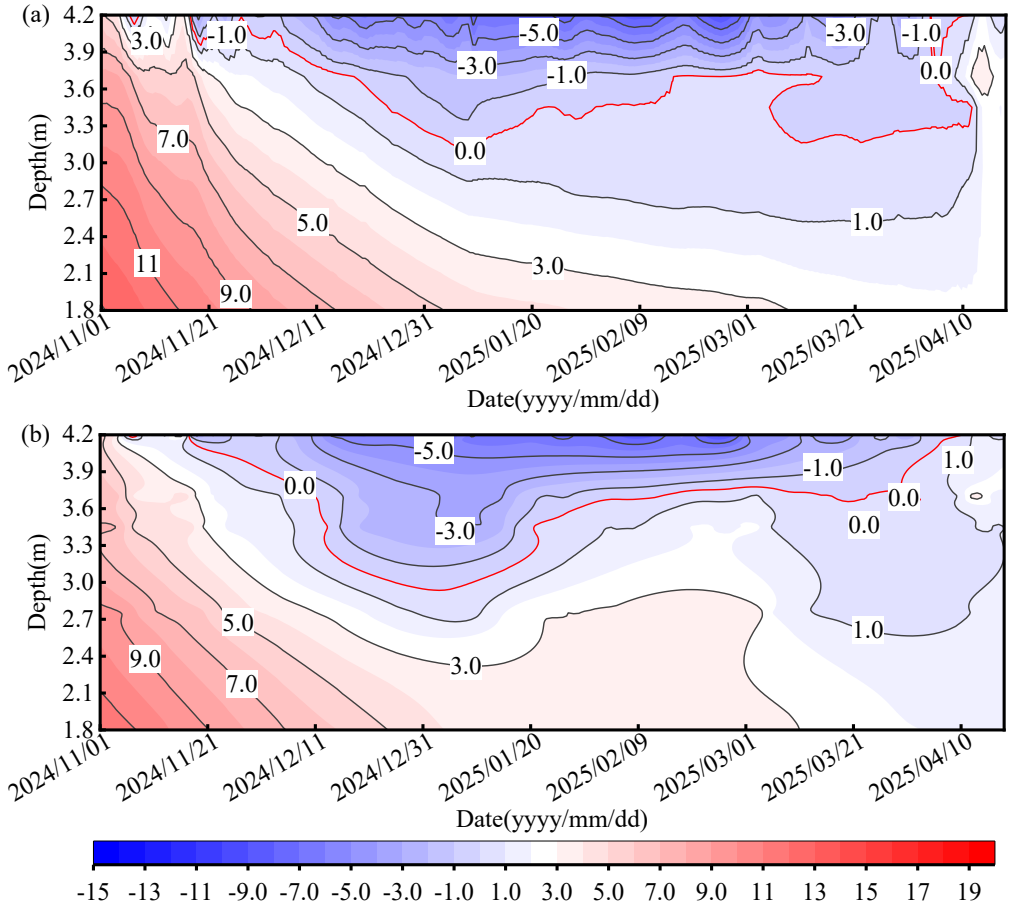

Fig. 18. Frost depth progression at TE1: (a) track center; (b) shoulder center.

5.2 Cross-section TE2 (midpoint between adjacent pipes HS3 and HS4)

Although TE2 was located midway between two adjacent pipes, where no direct heating element was installed, field data showed clear evidence of thermal influence due to lateral diffusion. For example, Fig. 19 shows that at 50 cm depth, soil temperatures increased by ≈0.2–4.4 °C across different lateral positions, following a temperature gradient away from the nearest pipe. At the track center, where the untreated soil remained at –2.7 °C, TE2 recorded values of –1.38 °C at 50 cm, –1.26 °C at 75 cm, +0.03 °C at 145 cm, and +3.7 °C at 245 cm, confirming that overlapping thermal fields extended protection to the inter-pipe zone.

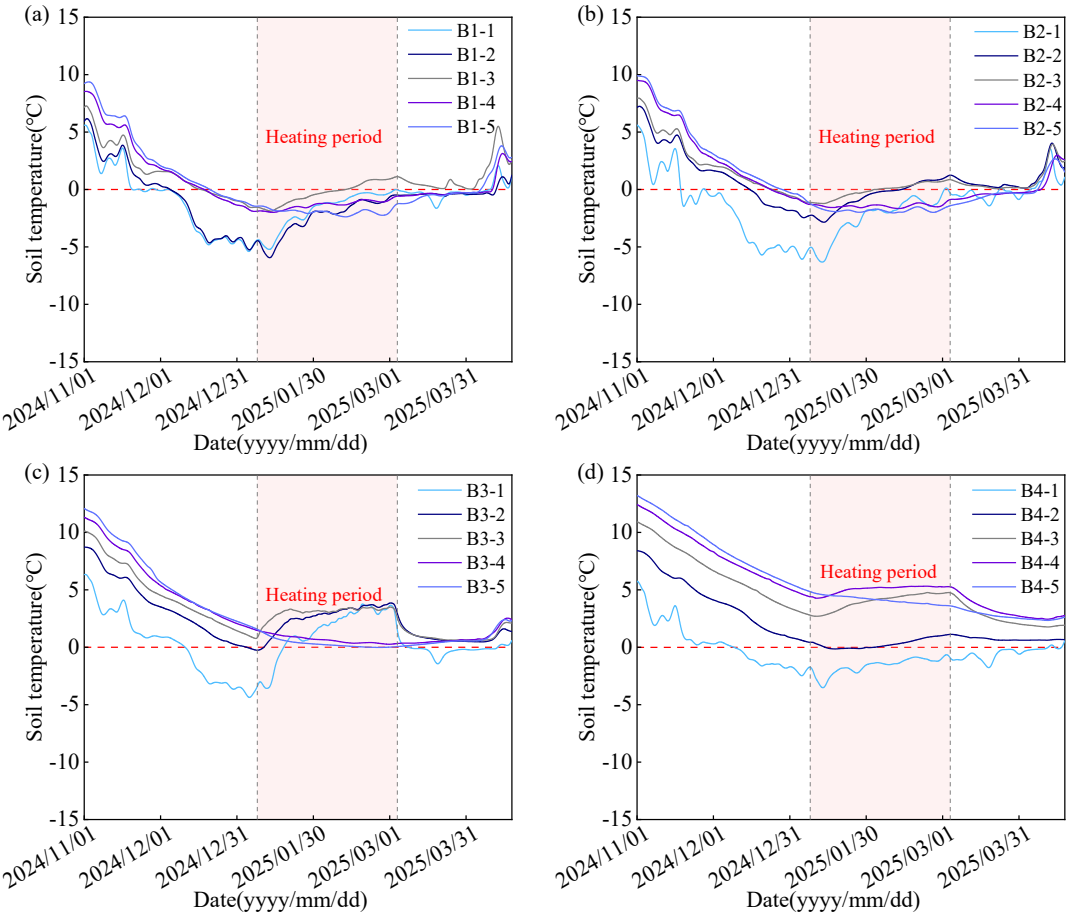

Fig. 19. Soil temperature variation at TE2 (midpoint between HS3 and HS4) at depths of (a) 50, (b) 75, (c) 145, and (d) 245 cm.

The thermal field in Fig. 20 reveals that while the strong elliptical heating plume observed at TE1 was absent, the isotherms at TE2 were nonetheless flattened, indicating a thermal-barrier effect. For example, on January 20, frost depths had stabilized at ≈87 cm (track center) and ≈80 cm (shoulder center), far shallower than in the untreated section. Similarly, on March 3, frost depths remained limited to ≈83 cm and ≈44 cm at the track center and shoulder center, respectively, only slightly deeper than those at TE1. Thus, the design spacing of 2.0 m between pipes ensured sufficient overlap to prevent deep frost penetration.

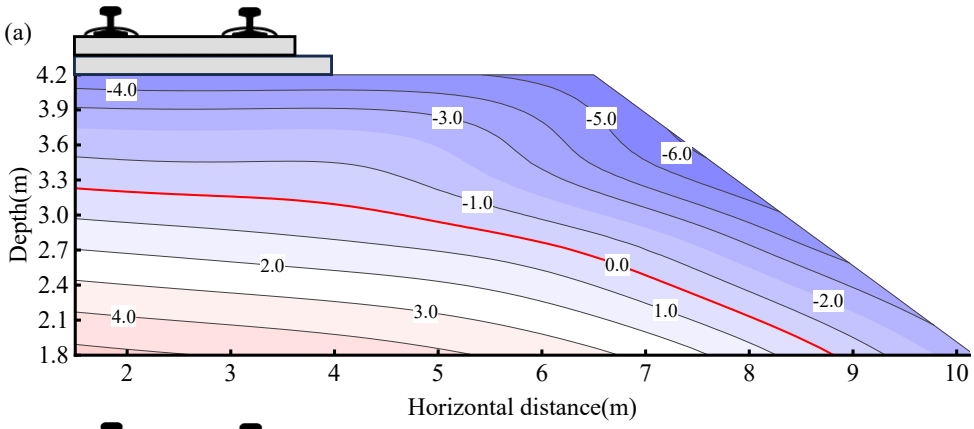

511

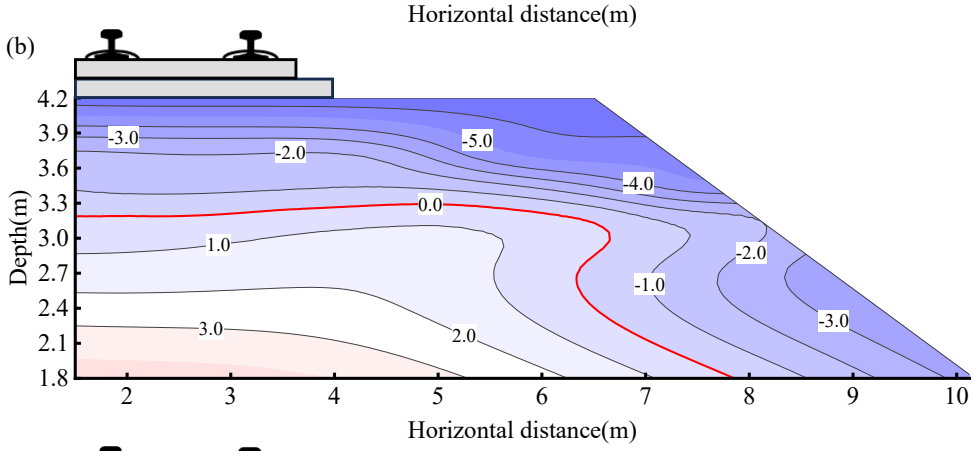

512

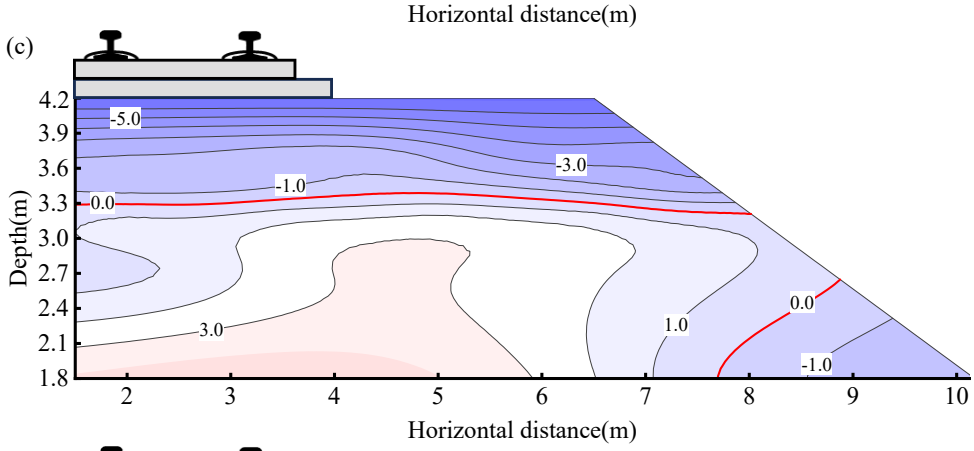

513

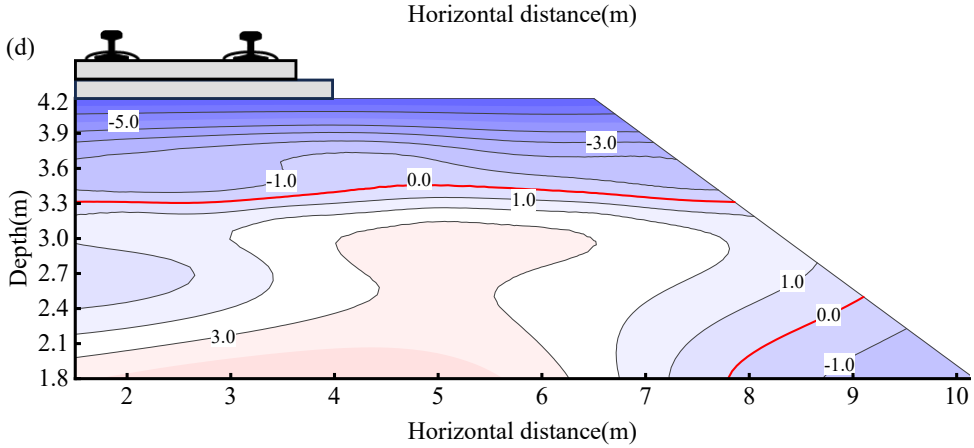

514

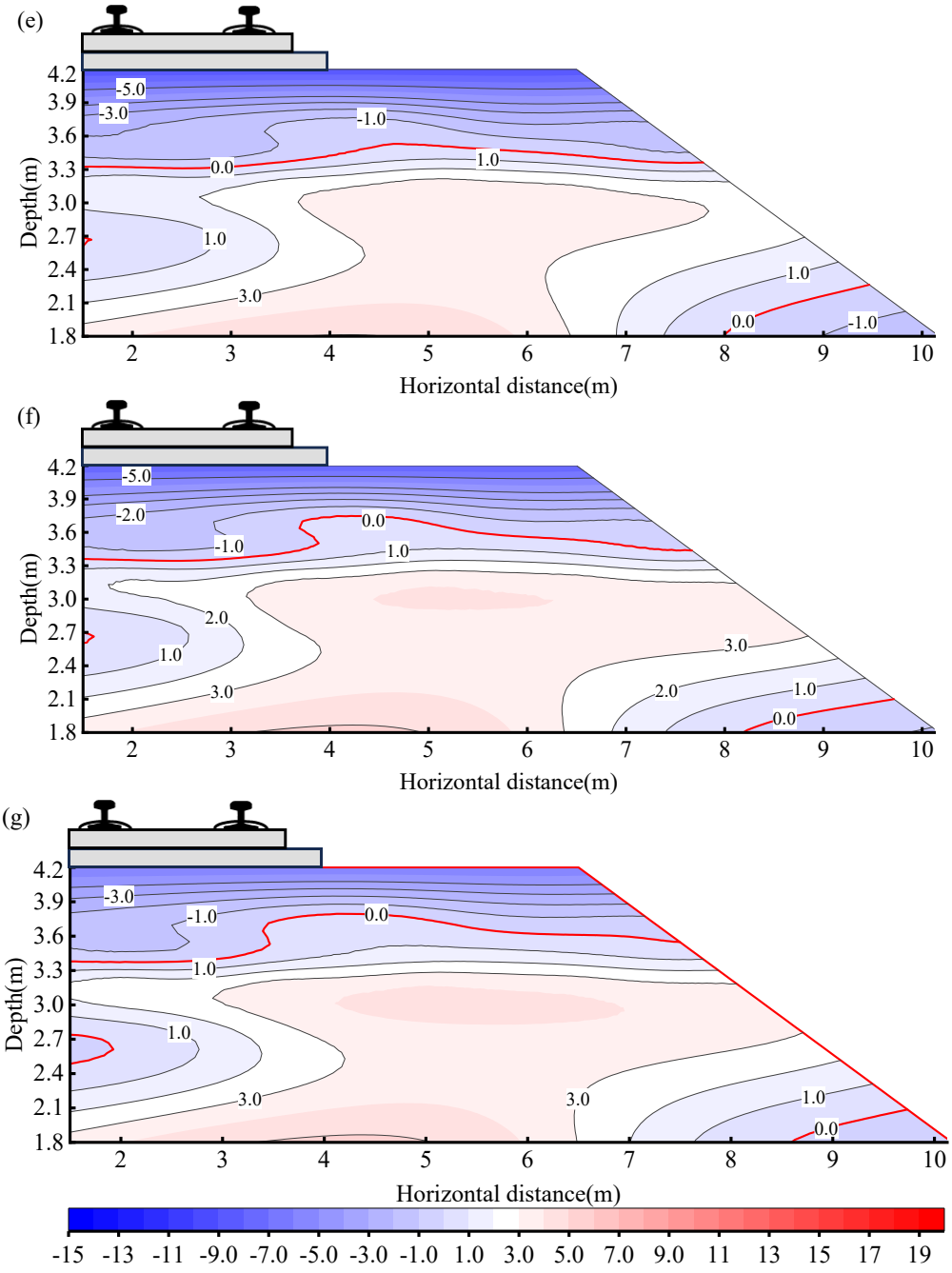

Fig. 20. Temperature field at TE2, highlighting the overlapping protection zone between adjacent supply pipes. (a) January 5, 2025; (b) January 10, 2025; (c) January 20, 2025; (d) January 30, 2025; (e) February 10, 2025; (f) February 20, 2025; (g) March 3, 2025.

Frost depth evolution (Fig. 21) also reflects the delayed but effective response. For example, because TE2 was located 1.0 m from the nearest pipe, frost depths continued

to deepen briefly after January 7 before reversing on January 10 at the shoulder and January 14 at the track center. By early February, frost depths had decreased to ≈92 cm and ≈77 cm, respectively. Complete thawing occurred on April 10, ≈9 days earlier than in the untreated subgrade, but ≈3 days later than at TE1. These findings confirm that the proper design of pipe spacing enables stable thermal coverage without unprotected cold zones, though the response at intermediate locations lags slightly behind the directly heated sections.

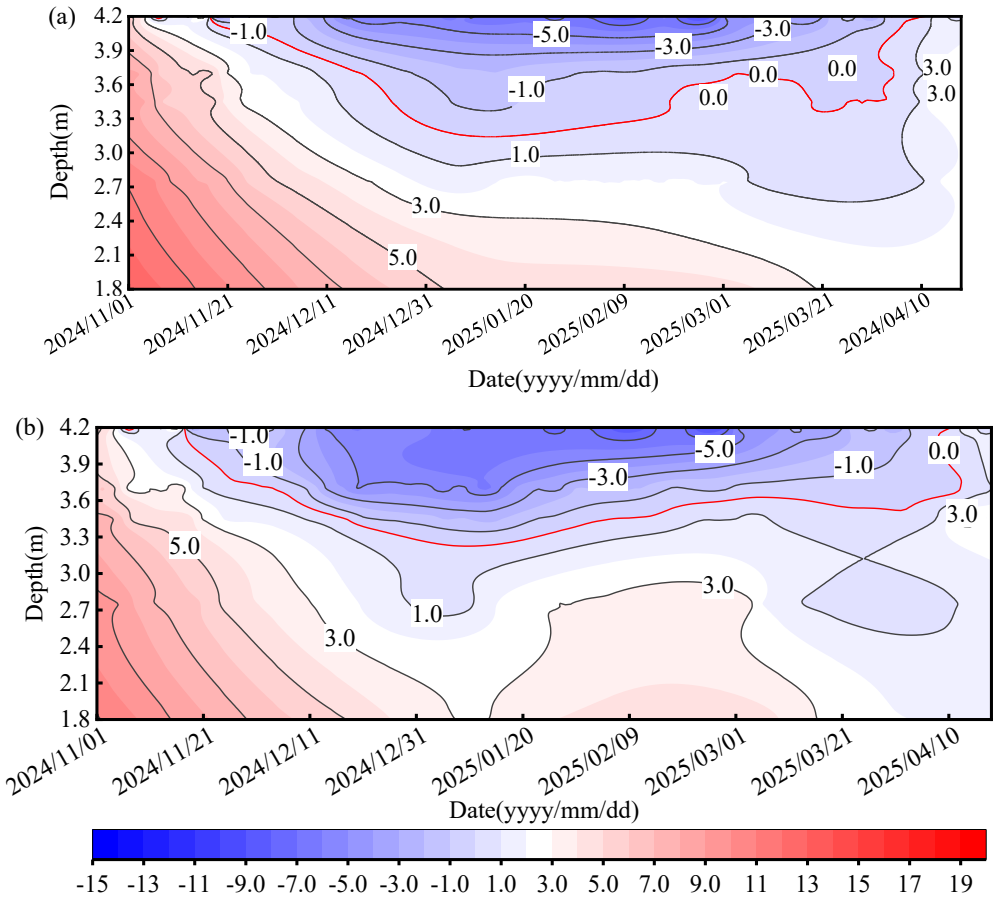

Fig. 21. Frost depth progression at TE2: (a) track center; (b) shoulder center.

5.3 Longitudinal section TE4 (between adjacent pipes HS3–HS4)

The thermal response along the longitudinal section TE4, midway between HS3 and HS4 at 95 cm depth, further demonstrates the spatial interaction of heating fields.

Fig. 22 shows that prior to heating (November to early January), soil cooled gradually to ≈0 °C at a rate of ≈0.13 °C/d, with little variation across measurement points. After activation on January 7, temperatures rose rapidly. Within 10 days, the soil had warmed to ≈5.0 °C at 20 cm from the pipe, ≈3.0 °C at 40 cm, ≈1.8 °C at 60 cm, and ≈0.8 °C at 80 cm, while the untreated soil at the same depth remained ≈ –1.7 °C. By January 19, the warming zones of HS3 and HS4 had fully overlapped, eliminating residual frozen segments between adjacent pipes.

After this initial surge, the heating effects continued to accumulate more slowly. By March 3, soil temperatures had increased by +7.2 °C at 20 cm, +5.2 °C at 40 cm, +4.5 °C at 60 cm, +4.4 °C at 80 cm, and +4.0 °C at 100 cm relative to the preheating conditions. This demonstrates that thermal coverage between adjacent pipes was complete, with no harmful residual freezing. When the pumps were turned off in early March, temperatures declined quickly, reflecting both the effectiveness and the timeliness of the active heating response.

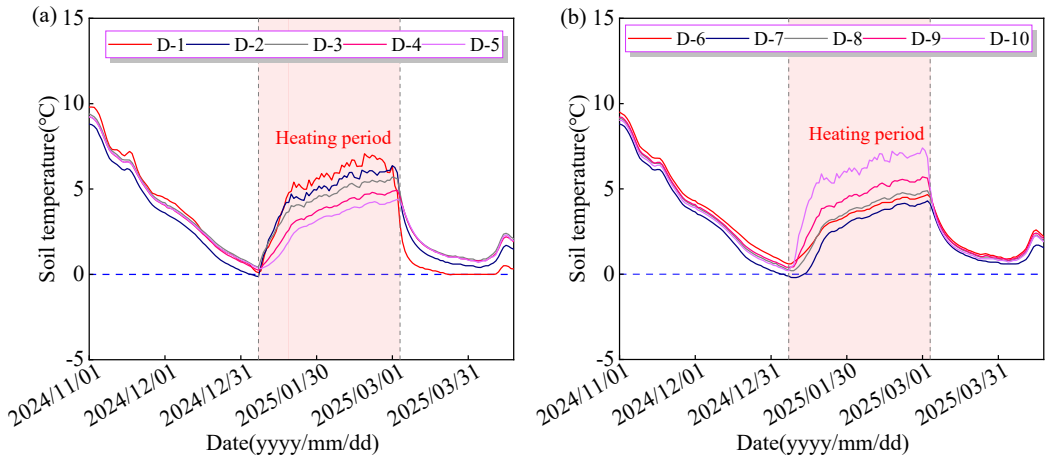

Fig. 22. Soil temperature evolution along longitudinal section TE4 between (a) HS3 and (b) HS4.

The longitudinal thermal field in Fig. 23 further illustrates this progression.

Initially, the 0 °C isotherm had an undulating pattern, dipping between the two pipes, which indicated deeper frost penetration in the inter-pipe zone. As heating continued, the isotherm rose and gradually flattened, showing the merging of adjacent heating plumes. By March 3, the depth difference between the two pipe locations had narrowed from 25 cm to ≈10 cm, effectively eliminating the risk of differential longitudinal frost heave. Nevertheless, the observed variation between sections TE1 and TE2 suggests that in full-scale applications, designers should carefully adjust both pipe spacing and operational parameters to minimize temperature disparities and maintain track smoothness.

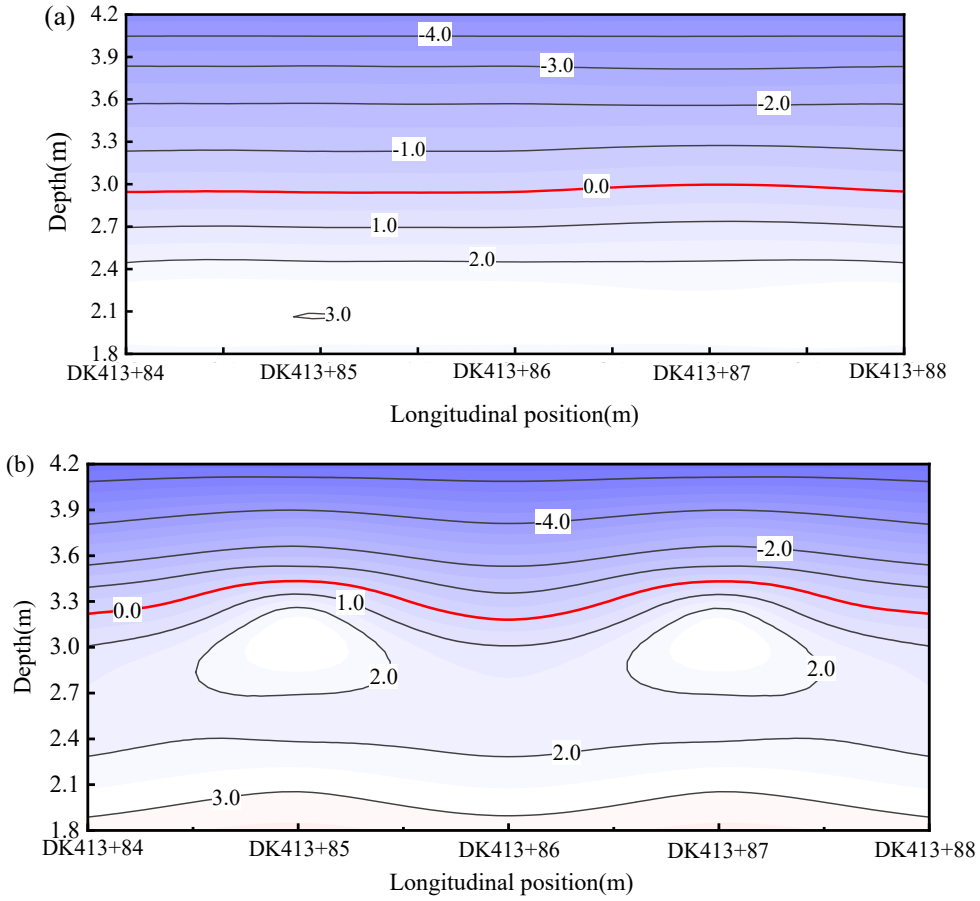

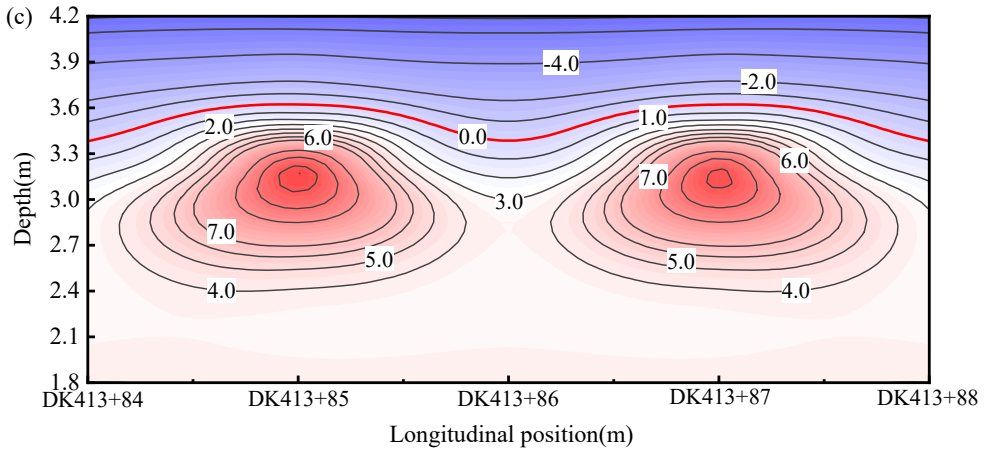

566

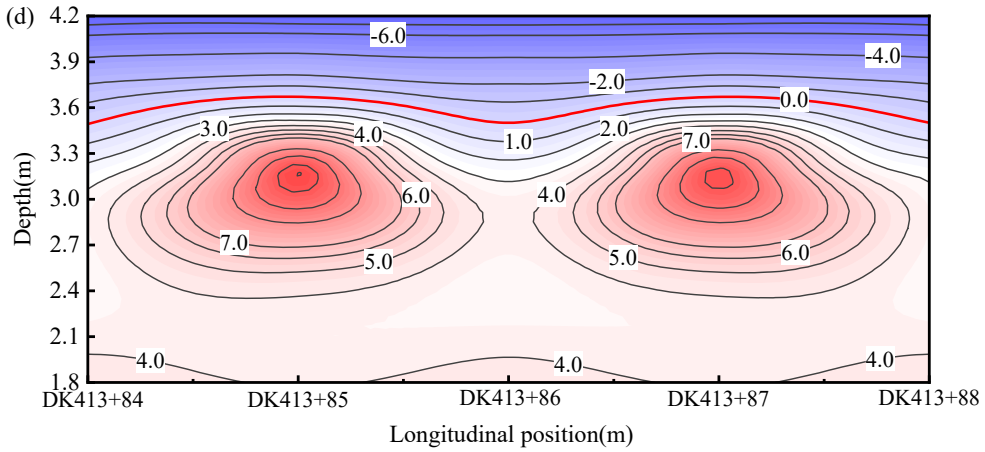

567

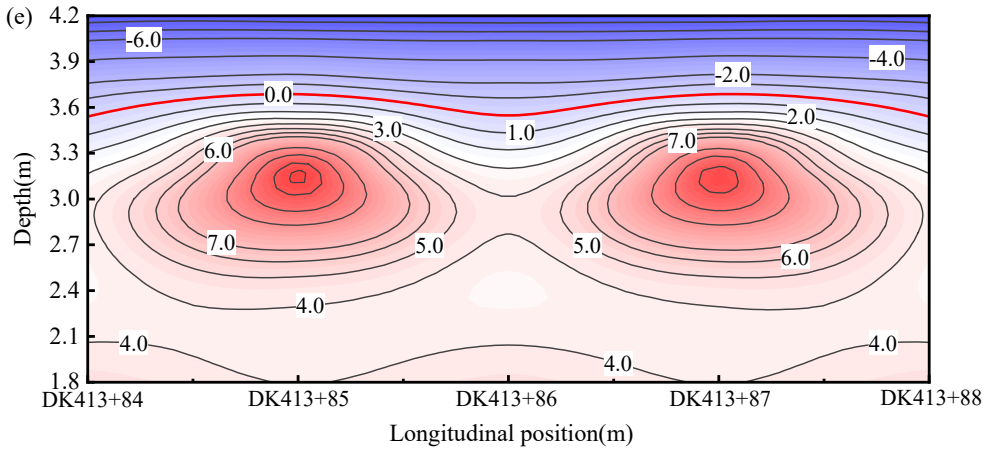

568

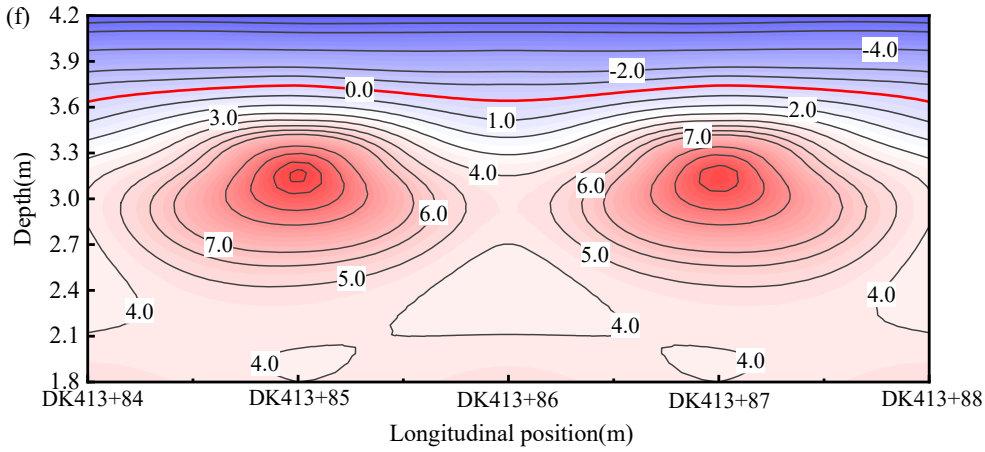

569

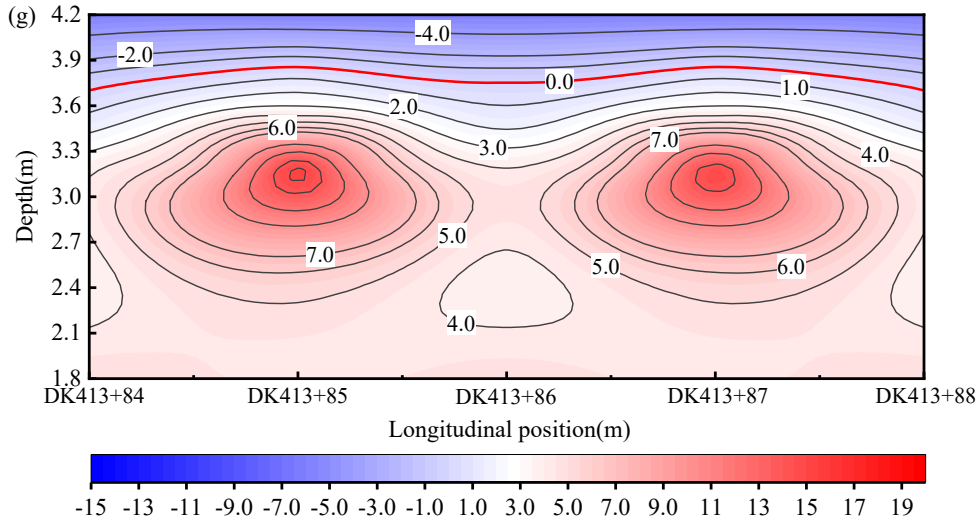

570

571 **Fig. 23.** Temperature field at longitudinal section TE4, illustrating merging of adjacent
572 heating plumes and elimination of frozen zones. (a) January 5, 2025; (b) January 10,
573 2025; (c) January 20, 2025; (d) January 30, 2025; (e) February 10, 2025; (f) February
574 20, 2025; (g) March 3, 2025.

575 ## 6. Discussion and Recommendations

576 The field results confirm that shallow geothermal energy, harnessed through
577 ground-source heat pumps, can reduce frost heave on high-speed railway subgrades.
578 Two main attributes of shallow geothermal energy make it especially suitable for this
579 application. First, it is efficient, renewable, and environmentally benign, consistent with
580 global goals of energy conservation and carbon reduction. Second, it is abundant and
581 regionally adaptable. In mid-latitude areas such as Northeast China, where seasonal
582 temperature differences are large, geothermal reserves can be readily used, with thermal
583 energy stored in summer and recovered in winter. This gradient-based usage, when
584 coupled with heat pump technology, reduces both energy transmission costs and the
585 difficulty of adapting infrastructure to severe climatic fluctuations.

586 However, for practical railway deployment, stakeholders are concerned not only

with effectiveness but also with long-term energy consumption and operational reliability. Field observations highlight three interrelated issues that must be addressed in future applications:

Effectiveness. The primary criterion is the degree to which frost penetration and extreme subgrade temperatures can be controlled. At the tested site, frost depths at the track center and shoulder center were reduced from ≈195 and ≈224 cm in the untreated subgrade to ≈70 and ≈34 cm in the heated section (TE1). The low-temperature extremes were also moderated, with several layers maintained above 0 °C. These results demonstrate that an active heat supply can establish a “thermal barrier” and protect against the harmful effects of frost heave. In design practice, the positioning and spatial uniformity of this thermal barrier require particular attention. More specifically, optimizing the longitudinal spacing, burial depth, and heating capacity of supply pipes is critical to ensure uniform protection across both transverse and longitudinal sections.

Energy efficiency. From the perspective of railway operators, energy savings are closely linked to cost-effectiveness. The tested system operated under an intermittent schedule (2.5 h on, 0.5 h off), maintaining stable outlet–inlet temperature differences of ≈7.8–14.3 °C and an average pipe temperature of ≈18.7 °C throughout the winter. This balance ensured adequate frost control while limiting unnecessary heat loss. In full-scale operations, it is recommended that the start–stop ratio be optimized dynamically based on real-time frost depth monitoring and climatic conditions. For severe frost events requiring rapid remediation, continuous operation may be justified; however, for long-term preventive operation, smaller start–stop ratios should be applied

to achieve both protection and energy conservation.

Reliability and durability. The long-term performance of the system depends on the stability of subsurface heat exchange and the robustness of equipment under extreme cold. Extended operation will inevitably lead to localized thermal saturation zones or soil heat buildup adjacent to heat-supply pipes, which may reduce efficiency. To mitigate this, materials with high thermal conductivity should be considered for backfilling between pipes and conduits, thereby enhancing heat dissipation into the surrounding soil. In addition, synergetic protection systems should be explored, combining external thermal insulation with internal heating. Such hybrid schemes would delay the infiltration of cold energy while reinforcing the protective barrier within the frost-susceptible zone of the subgrade.

In summary, three key aspects should guide the design and implementation of subgrade heat pump systems: (1) effectiveness, achieved by controlling frost depth and extreme low temperatures through optimized system layout; (2) energy efficiency, ensured by adjusting operation schedules to minimize heat losses while maintaining adequate protection; and (3) long-term reliability, which depends on durable equipment, efficient heat diffusion, and integration with complementary thermal insulation measures. Addressing these aspects through continued research and field trials will be essential for translating pilot demonstrations into large-scale engineering practice.

7. Conclusions

This study conducted a full-scale field experiment on the Shenyang–Baishan high-speed railway to evaluate the performance of a ground-source heat pump system for

631 active frost-heave prevention in a seasonally frozen region of Northeast China. A 20 m-
632 long test section was constructed with horizontally embedded heat-supply pipes and
633 vertically drilled collector pipes. It's thermal and deformation responses were
634 compared against an untreated subgrade during the severe winter of 2024–2025. Based
635 on the results, the following conclusions were drawn:

636 1. Severity of natural frost action. The untreated subgrade in the Changbai
637 Mountain region experienced frost depths of ≈195 cm at the track center and
638 ≈224 cm at the shoulder center, with extreme soil temperatures of –3.8 °C (track
639 center) and –8.8 °C (shoulder) at 0.5 m depth. The frost duration exceeded 150
640 days, and the maximum rail heave reached 6.6 mm, surpassing the allowable
641 limit stipulated in high-speed railway standards. These observations confirm the
642 inadequacy of conventional passive measures in such an environment.
643 2. Heat pump effectiveness. The proposed geothermal heat pump system
644 successfully established a thermal barrier within the subgrade. Under
645 intermittent operation (2.5 h on : 0.5 h off), outlet–inlet temperature differences
646 remained stable (≈7.8–14.3 °C), and the supply pipe maintained an average fluid
647 temperature of ≈18.7 °C throughout winter. As a result, frost depths were limited
648 to ≈70 cm (track center) and ≈34 cm (shoulder center) at TE1, while no harmful
649 frost heave was recorded in the heated section.
650 3. Spatial coverage and diffusion**.** Both directly heated sections (TE1) and
651 intermediate zones (TE2 and TE4) exhibited substantial thermal improvement.
652 Overlapping heat plumes between adjacent pipes prevented the formation of

"thermal cold gaps". Even at the midpoints between pipes, frost depths were suppressed to ≈83 cm (center center) and ≈44 cm (shoulder center), demonstrating that a pipe spacing of 2.0 m provided adequate protection.

4. Implications for design and operation. The system not only reduced frost depth and moderated extreme temperatures but also advanced thaw onset in the heated section by ≈12 days relative to the control. To maximize performance while limiting energy use, operating schedules should ideally be optimized in real-time based on climatic conditions and monitored frost development. Long-term reliability requires enhanced backfill thermal conductivity, prevention of localized heat accumulation, and possible integration with external insulation measures.

5. Engineering significance. This study demonstrates, for the first time, that ground-source heat pump technology can be applied to ballastless high-speed railway subgrades to minimize frost-heave related deformation. The approach provides a promising alternative to conventional passive measures, aligning with low-carbon and energy-efficient infrastructure goals. Further refinement of design parameters and long-term monitoring is necessary to enable broader implementation on transport systems in cold-regions.

Declaration of Competing Interests

The authors declare that they have no known competing financial interests or personal relationships that could have influenced the work reported in this paper.

Acknowledgments

This work was supported by the National Natural Science Foundation of China (Grant Nos. 52572377, U2469206) and the Natural Science Foundation of Hebei Province (Grant Nos. E2023210064, 24465001D).

Data Availability

The datasets generated and/or analyzed during the current study are available from the corresponding author on reasonable request.

References

[1] Qin YT, Cai GQ, Liu QQ, Su YL, Li J. Investigation on frost heave characteristics of red-stratum mudstone for HSR subgrade based on the orthogonal array testing. Cold Reg Sci Technol 2025; 238: 104559. https://doi.org/10.1016/j.coldregions.2025.104559.

[2] Lai YM, Zhang SM, Yu WB. A new structure to control frost boiling and frost heave of embankments in cold regions. Cold Reg Sci Technol 2012; 79-80: 53-66. https://doi.org/10.1016/j.coldregions.2012.04.002

[3] He HS, Teng JD, Zhao SW, Guan W, Zhang S. Comparative evaluation of the methods of assessing frost heave susceptibility. Cold Reg Sci Technol 2025; 231: 104406. https://doi.org/10.1016/j.coldregions.2024.104406.

[4] Li JF, Wang ZL, Teng JD, Zhang S. Numerical prediction of frost heave in soils: The role of the ice lens initiation criterion. Comput Geotech 2025; 177: 106833. https://doi.org/10.1016/j.compgeo.2024.106833.

[5] Zhang LH, Shi YJ, Yang CS, Ma W, Han DW, Shang F, Chen C, Yang YZ. Water accumulation unrelated to ice segregation near the freezing front during soil freezing: Implications for frost heave in high-speed railway embankments and ground ice formation. Catena 2024; 243: 108189. https://doi.org/10.1016/j.catena.2024.108189.

[6] Zhu HH, Jiang ZH, Li L. Projection of climate extremes in China, an incremental

exercise from CMIP5 to CMIP6. Sci Bull 2021; 66(24): 2528–2537. https://doi.org/10.1016/j.scib.2021.07.026.

[7] Miao Q, Niu FJ, Lin ZJ, Luo J, Liu MH. Comparing frost heave characteristics in cut and embankment sections along a high-speed railway in seasonally frozen ground of Northeast China. Cold Reg Sci Technol 2020; 170: 102921. https://doi.org/10.1016/j.coldregions.2019.102921.

[8] Chen W, Zhang YS, Zhang TQ, Wang WD, Lou P, Pan ZL. Consideration of the effects of frost heave force and train loads on the cracks and propagation pattern of ballastless track slabs in cold regions. Cold Reg Sci Technol 2024; 224: 104233. https://doi.org/10.1016/j.coldregions.2024.104233.

[9] Deng F, Lu JG, Wan XS, Liu BS, Zhang BL, Fu H. Mitigating frost heave of a soil stabilized with sisal fiber exposed to freeze–thaw cycles. Geotext Geomembranes 2025; 53(1): 394–404. https://doi.org/10.1016/j.geotexmem.2024.10.005.

[10] Lu JG, Deng F. Pei WS, Wan XS, You ZL, Zhang ZX. Mitigating frost heave and enhancing mechanical performance of silty clay with sisal fibre and geopolymer. Constr Build Mater 2024; 447: 138120. https://doi.org/10.1016/j.conbuildmat.2024.138120.

[11] Zhang MY, You ZL, Pei WS, Zhang Z, Melnikov A, Luo T. Mitigating embankment frost heave with nano-ZnO in the Arctic. J Clean Prod 2023; 393: 136073. https://doi.org/10.1016/j.jclepro.2023.136073

[12] Wang YF, Wu YK, Li X, Wei SW, Yan HY. Experimental investigation of the capillary drainage performance of multilayer wicking fabric. Geotext Geomembranes 2025; 53(5): 1168–1183. https://doi.org/10.1016/j.geotexmem.2025.05.005.

[13] Hao XY, Ma W, Feng WJ, Wen Z, Zhang LH. The mechanism of hydraulic pressure aggravates coarse-grained soil frost heave: Implication for frost prevention to high-speed railway subgrade. Transp Geotech 2025; 52: 101590. https://doi.org/10.1016/j.trgeo.2025.101590.

[14] Zhang D, Li X, Li XK, Zheng SF, Liu AQ, Wang M. Experimental study on the influence of initial water saturation on segregation frost-heaving behavior in silty

731 clay columns. Appl Therm Eng 2023; 234: 121236.
732 https://doi.org/10.1016/j.applthermaleng.2023.121236.
733 [15] Oyeyi AG, Badewa EA, Ni FM, Tighe S. Field study on thermal behavior of
734 lightweight cellular concrete as pavement subgrade protection in cold regions.
735 Cold Reg Sci Technol 2023; 214: 103966.
736 https://doi.org/10.1016/j.coldregions.2023.103966.
737 [16] Zhang KY, Ren JJ, Du W, Luo L, Liu JG, Deng SS. Thermal insulation
738 performance and dynamic response of anti-freeze subgrade of high-speed railway
739 in seasonally frozen regions. Transp Geotech 2023; 42: 101081.
740 https://doi.org/10.1016/j.trgeo.2023.101081.
741 [17] Mao WJ, Ma B, Xu JY. Phase change material coated geotextile for temperature
742 regulation of subgrade soil. J Energy Storage 2024; 81: 110438.
743 https://doi.org/10.1016/j.est.2024.110438.
744 [18] Zhao Y, Lu Z, Liu J, Tang CX, Tabaroei A, Zhang R, Feng YN, Yao HL.. A novel
745 approach to water–salt migration prevention: foamed lightweight soil barrier layer
746 technology. Cold Reg Sci Technol 2025; 236: 104514.
747 https://doi.org/10.1016/j.coldregions.2025.104514.
748 [19] Liu DH, Zheng H. Numerical simulation of the anti-freezing performance of a
749 phase change clay core-wall with loose covering. Appl Therm Eng 2023; 233:
750 121042. https://doi.org/10.1016/j.applthermaleng.2023.121042.
751 [20] Xu K, Chen Z, Xiao HL, Zheng LF, Wang JM. Analysis of entransy dissipation
752 thermal resistance and heat transfer efficiency of electrical heating snow-melting
753 pavement. Therm Sci Eng Prog 2025; 61: 103551.
754 https://doi.org/10.1016/j.tsep.2025.103551.
755 [21] Ma ZP, Wei HB, Wei DS, Jiang BY, Wang XF. Study on snow melting performance
756 evaluation and optimization design of conductive rubber electric heating pavement.
757 Constr Build Mater 2025; 470: 140556.
758 https://doi.org/10.1016/j.conbuildmat.2025.140556.
759 [22] Wang F, Fu CL, Liu K, Huang SL, Gao YM, Xie HZ. Experimental study and
760 numerical simulation of concrete pavement electrical heating for snow melting.

761 Constr Build Mater 2024; 442: 137611.
762 https://doi.org/10.1016/j.conbuildmat.2024.137611.
763 [23] Zhang WQ, Dong SF, Song ZX, Ding SX, Yi JY, Han BG. Snow-melting
764 performance and application method of stainless steel wires-modified conductive
765 asphalt concrete based on electrothermal conversion. Appl Therm Eng 2025; 269:
766 126066. https://doi.org/10.1016/j.applthermaleng.2025.126066.
767 [24] Ma ZP, Wei HB, Wei DS, Jiang BY, Wang XF. Heat transfer characteristics and
768 preheating time prediction of conductive rubber active snow melting bridge deck.
769 Appl Therm Eng 2025; 265: 125604.
770 https://doi.org/10.1016/j.applthermaleng.2025.125604.
771 [25] Rahman ML, Malakooti A, Ceylan H, Kim S, Taylor PC. A review of electrically
772 conductive concrete heated pavement system technology: From the laboratory to
773 the full-scale implementation. Constr Build Mater 2022; 329: 127139.
774 https://doi.org/10.1016/j.conbuildmat.2022.127139.
775 [26] Xu HN, Wang DW, Tan YQ, Zhou J, Oeser M. Investigation of design alternatives
776 for hydronic snow melting pavement systems in China. J Clean Prod 2018; 170:
777 1413–1422. https://doi.org/10.1016/j.jclepro.2017.09.262.
778 [27] Yu ZH, Zhang GZ, Cui HZ, Wang ZT, Cao ZM.. A cross-season antifreeze system
779 utilizing tunnel lining GHEs and solar energy: Performance and effect mechanism
780 at various environmental parameters. Renew Energ 2025; 242: 122428.
781 https://doi.org/10.1016/j.renene.2025.122428.
782 [28] Jiao WX, Paste AK. Experimental investigation of inclination angle on the snow
783 melting process of heated pavement. Cold Reg Sci Technol 2023; 205: 103704.
784 https://doi.org/10.1016/j.coldregions.2022.103704.
785 [29] Hong W, Liu KJ, Yan LC, Song SL, Cao YK, Gao HG. Reliable testing of snow
786 and ice melting on road using a multifunctional experimental setup. Constr Build
787 Mater 2025; 470: 140623. https://doi.org/10.1016/j.conbuildmat.2025.140623.
788 [30] Kugler T, Mustafa M, Moormann C. Geothermal hydronic pavement heating and
789 cooling systems using tunnel geothermal energy. Tunn Undergr Sp Tech 2025; 164:

106812. https://doi.org/10.1016/j.tust.2025.106812.

[31] Zhang Y, Xia CC, Zhou SW, Xu KW, Cao SP, Peng WB, Zhang JX. Effect of intermittent operation on the thermal performance of a solar seasonal thermal storage heating system in a cold-region tunnel. Renew Energ 2025; 244: 122667. https://doi.org/10.1016/j.renene.2025.122667.

[32] Gerola M, Cecinato F, Haasnoot JK, Vardon PJ. The role of design and site-dependent parameters in the thermal performance of energy quay walls. Energy 2025; 325: 135990. https://doi.org/10.1016/j.energy.2025.135990.

[33] Zhang XY, Chen L, Sheng Y, Huang L, Ming F, Peng CY. Modeling mechanical behavior of buried pipe suffering from frost-heaving force based on the Winkler elastic foundation beam theory. Transp Geotech 2024; 49: 101425. https://doi.org/10.1016/j.trgeo.2024.101425.

[34] Liu JK, Sun ZH, Cui YH, Hu TF, Tai BW. Dynamic mechanical characteristics and anti-thaw measures of warm frozen soil. Transp Eng 2025; 20: 100346. https://doi.org/10.1016/j.treng.2025.100346.

[35] Zhang JY, He ZL, Feng J. Frost damage improvement for railway subgrade based on ground temperature control in cold regions. KSCE J Civ Eng 2021; 25(8): 2911–2921. https://doi.org/10.1007/s12205-021-2197-9.

[36] Zhang WQ, Wen Z, Wang D, Guo L, Su FY, Wang XB, Yu QH. Numerical modelling and mechanism of water–heat–deformation of subgrade under heating effect in cold regions. Int Commun Heat Mass 2025; 164: 108911. https://doi.org/10.1016/j.icheatmasstransfer.2025.108911.

[37] Zhang WQ, Wang D, Guo L, Wen Z, Yu QH. Study on the mitigation effect and mechanism of solar heating subgrade system on frost heave of railway subgrade in cold regions. Renew Energ 2024; 237: 121909. https://doi.org/10.1016/j.renene.2024.121909.

[38] Hu TF, Zhao LQ, Wang TF, Yue ZR, Yuan YF, Zhang YM. Geothermal heat pump solutions for frost heave control in railway subgrades. Geothermics 2025; 127: 103244. https://doi.org/10.1016/j.geothermics.2024.103244.

[39] Hu TF, Wang L, Wang TF, Sun TC, Li TF. Frost-resistant embankments with a

novel ground source heat pump system. Res Cold Arid Reg 2024; 16(6): 292–301. https://doi.org/10.1016/j.rcar.2024.10.002.

[40] Hu TF, Zhao LQ, Wang TF, Yue ZR, Yuan YF. Predictive modeling for dynamic heat load in frigid railway roadbeds: An energy-efficient approach. Therm Sci Eng Prog 2024; 56: 103049. https://doi.org/10.1016/j.tsep.2024.103049.